Structures 70 (2024) 107563

Contents lists available at ScienceDirect

Structures

journal homepage: www.elsevier.com/locate/structures

Nonlinear transient deflections of multi-layer sector plate structures on auxetic concrete foundation: Introducing an artificial intelligence algorithm for nonlinear problems

Peixi Guo [a,*], Yao Zhang [b], Yu Xi [b], Kashif Saleem [c], Mohammed El-Meligy [d,e], Hamed Safarpour [f]

[a] *Xijing University, Xi'an, Shaanxi 710123, China*
[b] *Shaanxi Key Laboratory of Safety and Durability of Concrete Structures, Xijing University, Xi' an 710123, China*
[c] *Department of Computer Science & Engineering, College of Applied Studies & Community Service, King Saud University, Riyadh 11362, Saudi Arabia*
[d] *Jadara University Research Center, Jadara University, PO Box 733, Irbid, Jordan*
[e] *Applied Science Research Center, Applied Science Private University, Amman, Jordan*
[f] *Independent Researcher*

A R T I C L E I N F O

Keywords:
Nonlinear transient deflections
Auxetic concrete foundation
Artificial intelligence algorithm
Multi-layer sector plates
FG-GOEM

A B S T R A C T

This paper presents a comprehensive study on the nonlinear transient deflections of multi-layer sector plates, with a focus on presenting an artificial intelligence algorithm for addressing nonlinear problems in structural mechanics using the datasets of mathematical simulation. Multi-layer sector plates, commonly used in various engineering applications, exhibit complex nonlinear behaviors under external loading, particularly when coupled with unconventional materials such as auxetic concrete foundations. In this study, we propose the use of a mathematical simulation to analyze the nonlinear transient deflections of multi-layer sector plates on an auxetic concrete foundation. After that, a dataset (approximately 3750 data) is obtained and the algorithm is trained to capture the intricate nonlinear responses of the structure under different loading conditions. By leveraging an artificial intelligence algorithm, the algorithm can accurately predict the nonlinear behaviors of the multi-layer sector plate system, including vibration characteristics, dynamic response, and stability analysis. Through extensive numerical and validation studies, we demonstrate the effectiveness of the current mathematical modeling in accurately capturing the nonlinear transient deflections of multi-layer sector plates on auxetic concrete foundations. Furthermore, the proposed machine learning algorithm offers a promising approach for addressing nonlinear problems in structural mechanics, providing a versatile and efficient tool for engineers to analyze and optimize complex structural systems. By integrating machine learning techniques into structural analysis, researchers can enhance the accuracy and efficiency of nonlinear transient deflection studies, paving the way for advancements in structural engineering and related fields.

1. Introduction

Composite materials are of significant importance to engineers due to their unique combination of properties, making them ideal for various applications [1]. First, their high strength-to-weight ratio allows for lighter yet stronger structures, crucial in aerospace, automotive, and civil engineering [2]. Second, composites offer excellent fatigue and corrosion resistance, leading to increased durability and reduced maintenance costs in harsh environments [3]. Third, their ability to be tailored for specific mechanical, thermal, and electrical properties makes them versatile for custom applications [4]. Fourth, composite materials enable engineers to design more efficient structures by optimizing material distribution and improving load-bearing capacity [5]. Fifth, their anisotropic nature allows for directional strength and stiffness, providing enhanced performance in specific loading conditions [6]. Sixth, engineers benefit from the ability to mold composites into complex shapes, facilitating innovative designs that would be difficult with traditional materials [7]. Seventh, the energy absorption capabilities of composites make them ideal for impact-resistant applications, improving safety in industries like automotive and defense [8]. Eighth, composites often have lower thermal conductivity, making them useful in thermal insulation applications, especially in energy-efficient systems

* Corresponding author.
E-mail address: 20190230@xijing.edu.cn (P. Guo).

https://doi.org/10.1016/j.istruc.2024.107563
Received 26 June 2024; Received in revised form 7 October 2024; Accepted 13 October 2024
Available online 23 October 2024

[9]. Lastly, the ease of integrating smart sensors into composite structures allows engineers to develop advanced monitoring systems, enhancing the functionality and longevity of modern infrastructure [10].

Stability analysis plays a crucial role in the measurement and understanding of the mechanical properties of various systems [11–14]. It serves as a foundation for predicting the behavior of materials and structures under different loading conditions, ensuring their reliability and safety. By assessing stability, engineers and researchers can determine the critical loads at which a system may fail or exhibit undesirable deformations, such as buckling or collapse [15,16]. This is particularly important in the design and construction of buildings, bridges, and other infrastructure, where stability analysis helps in identifying potential weaknesses and optimizing the structural design to withstand various forces [17]. Moreover, stability analysis provides insights into the material's response to dynamic loads, such as vibrations and shocks, which are essential for applications in aerospace, automotive, and other high-performance industries [18]. In addition to ensuring structural integrity, stability analysis is vital for advancing material science and engineering [19]. It enables the characterization of new materials, such as composites and nanocomposites, by providing a deeper understanding of their mechanical properties and behavior under different environmental conditions [20]. This knowledge is essential for developing innovative materials with enhanced performance characteristics, such as higher strength-to-weight ratios, better durability, and improved resistance to external factors [21,22]. Furthermore, stability analysis contributes to the refinement of computational models and simulation techniques, leading to more accurate predictions of material behavior [23]. As a result, it supports the ongoing development of advanced engineering solutions and contributes to the overall progress in the field of materials science and engineering [24].

Higher-order shear deformation theories (HSDTs) are critical for accurately estimating the displacement fields of structures, especially those composed of composite materials [25]. Unlike classical theories, HSDTs account for the shear deformation effects, which are significant in thick structures where shear deformations are not negligible [26]. By incorporating higher-order terms, these theories provide a more refined and precise prediction of the displacement fields, crucial for engineering applications requiring high accuracy [27]. One of the main advantages of HSDTs is their ability to capture the variation of transverse shear strains across the thickness of the structure [28]. This is particularly important for composite materials and multi-layer structures, which often exhibit complex shear behavior [29]. Traditional theories, such as the classical theory (CT) or first-order shear deformation theory (FSDT), can lead to inaccuracies in such cases as they oversimplify the shear deformation distribution [30]. HSDTs enhance the understanding of the structural behavior under various loading conditions, including static, dynamic, and thermal loads [31]. They provide a comprehensive framework for analyzing the response of structures to these loads, ensuring that the predictions are reliable and robust [32]. This is especially important for the design and analysis of critical components in aerospace, automotive, and civil engineering, where structural failure can have catastrophic consequences [33,34]. Furthermore, HSDTs improve the prediction of stress distributions within the structure [35,36]. Accurate stress estimation is essential for assessing the safety and durability of the material, as it helps identify potential failure points and regions with high-stress concentrations [37,38]. This information is invaluable for optimizing the design to enhance the overall performance and longevity of the structure [39,40]. The use of HSDTs also facilitates the development of more efficient and cost-effective designs [41]. By providing a deeper understanding of the displacement and stress fields, engineers can make informed decisions about material selection, thickness optimization, and reinforcement strategies [42]. This leads to structures that are not only stronger and more resilient but also lighter and more economical [43]. In summary, higher-order shear deformation theories are indispensable for accurately estimating the displacement fields of structures [44]. They offer a significant improvement over classical theories by accounting for the complexities of shear deformation, leading to more precise predictions of structural behavior [45]. This accuracy is crucial for ensuring the safety, performance, and efficiency of modern engineering structures [46]. Sectorial plates are extensively used in various engineering structures, including fundamental structural parts, curving bridge decks, building floor slabs, and steam turbine diaphragms, because of their great load-carrying capacity and design flexibility [47]. Utilizing FSDT and single-term EKM, Fallah et al. [48] performed bending analysis on one-layer functionally graded annular circular sector plates with arbitrary boundary conditions that were exposed to both uniform and non-uniform loadings. Ref. [48] and the references therein for a summary of linear bending studies of homogeneous and one-layer FG sector plates. As far as the authors are aware, no paper has been published on the linear bending analysis of FG multi-layer sector plates.

An overview of works on the nonlinear behavior of multi-layer, composite, and homogeneous sector plates is presented here. The elastic large deflection behavior of homogeneous sector plates was investigated by Turvey et al. [49] and Salehi et al. [50] utilizing non-linear von Kármán assumptions and a dynamic relaxation approach combined with a finite-difference discretization. Nath et al. [51] derived the governing equations of equilibrium for moderately thick homogeneous sector plates based on the FSDT and von-Karman kind of geometric non-linearity. They coupled an iterative incremental technique based on the Newton-Raphson method for the solution with the Chebyshev polynomials for the spatial discretization of the differential equations. Golmakani et al. [52] investigated the nonlinear bending behavior of solid/annular sector plates that were resting on a two-parameter elastic foundation and had moderate thickness and radially functionally graded. The sector plates were exposed to both uniform and non-uniform transverse loads. They used the dynamic relaxation approach in conjunction with the finite difference discretization methodology to solve the governing equations, which were derived based on the FSDT and non-linear von Kármán assumptions. Nonlinear bending analysis was carried out by Alinaghizadeh et al. [53] on two-directional functionally graded circular/annular sector plates with varied thicknesses that were sitting on a nonlinear elastic basis. The equilibrium equations were solved by means of the Newton-Raphson iterative technique and extended differential quadrature, drawing on von Kármán's geometric non-linearity and higher-order shear deformation theory. Alinaghizadeh et al. [54] used the generalized differential quadrature method in conjunction with the Newton-Raphson iterative scheme to investigate the nonlinear bending behavior of radially FG sector plates resting on elastic foundation. Their research was based on the FSDT and the von Kármán type of nonlinear geometry.

Multi-layer sector plates, especially those incorporating graphene origami-enabled auxetic metamaterial face sheets, exhibit lightweight yet robust characteristics ideal for aerospace applications. These structures can be utilized in aircraft components, satellites, and protective armor, where weight reduction and impact resistance are critical factors for performance and fuel efficiency. In this work, as the first work, nonlinear transient deflections of multi-layer sector plate on auxetic concrete foundation via both artificial intelligence algorithm and mathematical simulation. Understanding and predicting the nonlinear transient deflections of multi-layer sector plates are crucial for ensuring their stability and performance in engineering applications. This paper presents a comprehensive approach aimed at addressing these challenges through the integration of advanced techniques. Specifically, we introduce the concept of graphene origami-enabled auxetic metamaterial face sheets, which enhance the mechanical properties and auxetic behavior of the structures. Moreover, we propose a hybrid deep neural network framework that combines the power of machine learning with mathematical datasets to accurately predict the nonlinear behavior of these structures under varying loading conditions. Through the integration of machine learning with traditional numerical methods, our approach enables efficient and accurate predictive modeling of complex structures, providing valuable insights for the design and optimization of auxetic concrete foundations and multi-layer sector plates in engineering applications. The novelties of this work can be categorized into 4 different scopes: 1- Presenting nonlinear motion equations of the multi-layer sector plate made of two graphene origami-enabled auxetic metamaterial face sheets. 2- Presenting improved higher-order theory based on a hyperbolic function for multi-layer sector plates under external excitation. 3- Presenting auxetic concrete foundation with a negative Poisson ratio as the external substrate of the presented sector plate under external excitation. 4- Presenting an improved hybrid machine learning algorithm to predict the nonlinear dynamic deflection of multi-layer sector plates. Finally, some recommendations are presented for improving the stability and efficiency of the presented multi-layer sector plate under external excitation.

2. Mathematical modeling

The multi-layer annular sector plate design is shown in Fig. 1, along with the relevant measurements. It consists of a copper core and auxetic metamaterial face sheets enabled via Graphene origami.

2.1. Graphene origami-enabled auxetic metamaterial face sheets

As can be observed in Fig. 2, the FG-GOEAM composite annular sector plates are built with changes in GOri content and GOri folding degree. The two patterns in Fig. 2A illustrate how the GOri content changes layer by layer in the thickness direction. Greater GOri content is indicated by a deeper hue, and the weight fraction (W_{Gr}) varies correspondingly. An isotropic, homogeneous metamaterial annular sector plate with evenly distributed GOri across all layers is shown by the U-W_{Gr} pattern. The outer surface layers have a larger concentration of GOri, as shown by the symmetric distribution of the X-W_{Gr} pattern. Furthermore, it is assumed that the GOri folding degree, which is determined by the H atom coverage (H_{Gr}) in the crease, would progressively vary in the thickness direction. An enhanced folding degree is the consequence of more hydrogen atoms being chemically bound to the creases of Gori, as shown by a higher value. As shown in Fig. 2B, this research looks at the U-H_{Gr} and X-H_{Gr} folding degree patterns of GOri. Whereas the X-H_{Gr} pattern depicts an FG metamaterial composite annular sector plate with pristine graphene scattered on the surfaces and GOri distributed in the center, the U-H_{Gr} pattern displays an isotropic homogeneous metamaterial annular sector plate.

For the two graphene content distribution patterns, the $V_{\mathrm{Gr}}(k)$ as the volume percentages of the k-th layer are determined by [55].

$$U-W_{\mathrm{Gr}j}:V_{\mathrm{Gr}j}(k)=V_{\mathrm{Gr}j} \tag{1}$$

$$X-W_{\mathrm{Gr}j}:V_{\mathrm{Gr}j}(k)=2V_{\mathrm{Gr}j}|2k-N_L-1|/N_L$$

where k runs from 1 to N_L, where N_L is the total number of layers, and where j = b and t. The weight fraction W_{Gr} may be converted to provide the volume fraction V_{Gr}.

$$V_{\mathrm{Gr}j}=\frac{\rho_{\mathrm{Cu}j}W_{\mathrm{Gr}j}}{\rho_{\mathrm{Cu}j}W_{\mathrm{Gr}j}+\rho_{\mathrm{Gr}j}(1-W_{\mathrm{Gr}j})} \tag{2}$$

$$V_{\mathrm{Gr}j}+V_{\mathrm{Cu}j}=1$$

where the volume fraction of copper is indicated by ρ_{Cu}, which represents the density of pure copper, and ρ_{Gr}, which represents the density of

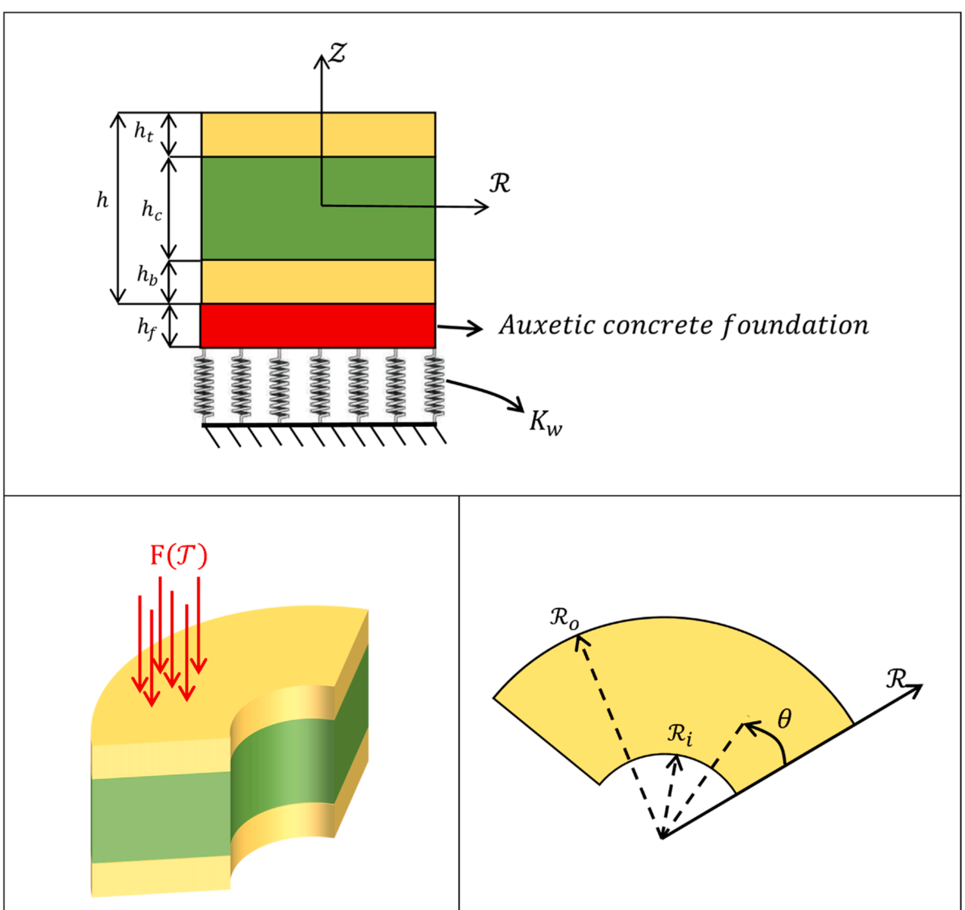

Fig. 1. Schematic of multi-layer annular sector plate on auxetic concrete foundation.

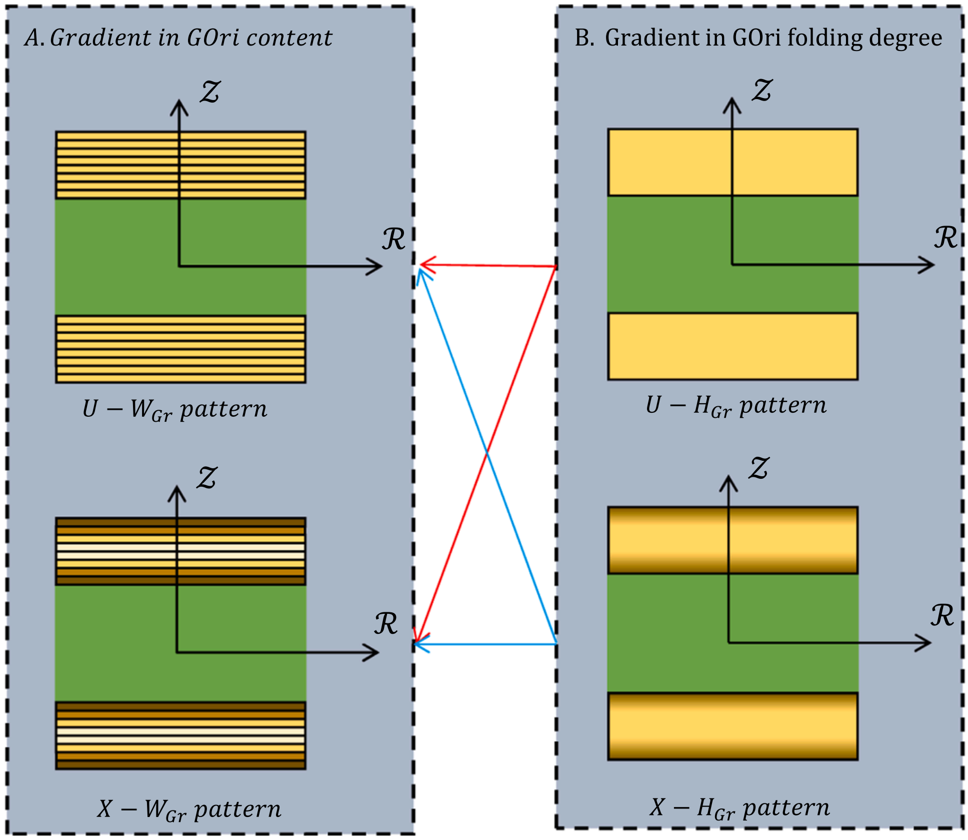

Fig. 2. Uneven sector plate and isotropic homogenous GOEAM annular sector with gradients in the degree of graphene folding and the amount of graphene (A and B).

graphene. Both a uniform and a non-uniform distribution along the thickness direction produce the H coverages $H_{\mathrm{Gr}}(\mathbb{z})$.

$$U - H_{\mathrm{Grt}} : H_{\mathrm{Grt}}(\mathbb{z}) = H_{\mathrm{Grt}}, \text{Face} - \text{sheet top} \tag{3}$$

$$U - H_{\mathrm{Grb}} : H_{\mathrm{Grb}}(\mathbb{z}) = H_{\mathrm{Grb}}, \text{Face} - \text{sheet bottom}$$

$$X - H_{\mathrm{Grt}} : H_{\mathrm{Grt}}(\mathbb{z}) = H_{\mathrm{Grt}}\cos\left(\frac{\mathbb{z} - 0.5h_c - 0.5h_t}{h_t}\pi\right), \text{Face} - \text{sheet top}$$

$$X - H_{\mathrm{Grb}} : H_{\mathrm{Grb}}(\mathbb{z}) = H_{\mathrm{Grb}}\cos\left(\frac{\mathbb{z} + 0.5h_c + 0.5h_b}{h_b}\pi\right), \text{Face} - \text{sheet bottom}$$

The Poisson's ratio (ϑ), Young's modulus (E), and density (ρ) of the material of GOEAMs are computed using the GP-assisted micromechanical models:

$$E_j = \frac{1 + \xi_j\eta_j V_{\mathrm{Gr}j}}{1 - \eta_j V_{\mathrm{Gr}j}} E_{\mathrm{Cu}j} \times f_{Ej}(H_{\mathrm{Gr}j}, V_{\mathrm{Gr}j}) \tag{4}$$

$$\vartheta_j = (\vartheta_{\mathrm{Gr}j} V_{\mathrm{Gr}j} + \vartheta_{\mathrm{Cu}j} V_{\mathrm{Cu}j}) \times f_{\nu j}(H_{\mathrm{Gr}j}, V_{\mathrm{Gr}j})$$

$$\rho_j = (\rho_{\mathrm{Gr}j} V_{\mathrm{Gr}j} + \rho_{\mathrm{Cu}j} V_{\mathrm{Cu}j}) \times f_{\rho j}(V_{\mathrm{Gr}j})$$

The following is the stated value of the coefficient of material (η) and size (ξ):

$$\eta_j = \frac{(E_{\mathrm{Gr}j}/E_{\mathrm{Cu}j}) - 1}{(E_{\mathrm{Gr}j}/E_{\mathrm{Cu}j}) + \xi_j} \tag{5}$$

$$\xi_j = 2(l_{\mathrm{Gr}j}/t_{\mathrm{Gr}j})$$

where the length and thickness of graphene are represented by the variables l_{Gr} and t_{Gr}, respectively; the modification functions $f_{E,\nu,\rho}(H_{\mathrm{Gr}}, V_{\mathrm{Gr}})$ are computed using the GP method, which is expressed as [56].

$$f_{Ej}(H_{\mathrm{Gr}j}, V_{\mathrm{Gr}j}) = 0.966 - 0.661 V_{\mathrm{Gr}j} - 5.5 H_{\mathrm{Gr}j} V_{\mathrm{Gr}j} + 38 H_{\mathrm{Gr}j} V_{\mathrm{Gr}j}^2 - 20.6 H_{\mathrm{Gr}j}^2 V_{\mathrm{Gr}j}^2 \tag{6}$$

$$f_{\vartheta j}(H_{\mathrm{Gr}j}, V_{\mathrm{Gr}j}) = 1.175 - 1.43 V_{\mathrm{Gr}j} - 17.9 H_{\mathrm{Gr}j} V_{\mathrm{Gr}j} + 16 H_{\mathrm{Gr}j}^2 V_{\mathrm{Gr}j}^2$$

$$f_{\rho j}(V_{\mathrm{Gr}j}) = 0.9969 - 2.01 V_{\mathrm{Gr}j}^2$$

Note that $T/T_0 = 1$ since ambient circumstances were taken into account [56]. The following are the relevant material properties of Cu, unless otherwise noted: At 300 K, the density (ρ_{Cu}) is 8.8 g/cm^3, Poisson's ratio (ϑ_{Cu}) is 0.387, and the Young's modulus (E_{Cu}) is 65.79 GPa. The material parameters of graphene are as follows: at 300 K, its density (ρ_{Gr}) is 1.8 g/cm^3, its Poisson's ratio (ϑ_{Gr}) is 0.220, and its elastic modulus (E_{Gr}) is 929.57 GPa. The geometric length of the graphene is 83.76 Å, and its thickness is 3.4 Å. Where Angstrom (Å) equal to 10^{-10} m.

3. Theoretical formulations

Mechab theory, a higher-order theory based on a hyperbolic function, is used to determine the sectoral and annular laminated plate's displacement field. Thus, the following is the displacement function of the laminated composite [57]:

$$\mathscr{U}_{\mathscr{R}}(\mathscr{R}, \theta, \mathscr{Z}, \mathscr{T}) = \mathscr{U}_{\mathscr{R}0}(\mathscr{R}, \theta, \mathscr{T}) + \mathbb{f}(\mathscr{Z})\mathfrak{T}_{\mathscr{R}} + \mathbb{g}(\mathscr{Z})\frac{\partial \mathscr{U}_{\mathscr{Z}0}}{\partial \mathscr{R}} \tag{7a}$$

$$\mathscr{U}_{\theta}(\mathscr{R}, \theta, \mathscr{Z}, \mathscr{T}) = \mathscr{U}_{\theta 0}(\mathscr{R}, \theta, \mathscr{T}) + \mathbb{f}(\mathscr{Z})\mathfrak{T}_{\theta} + \mathbb{g}(\mathscr{Z})\frac{\partial \mathscr{U}_{\mathscr{Z}0}}{\mathscr{R}\partial \theta} \tag{7b}$$

$$\mathscr{U}_{\mathscr{Z}}(\mathscr{R}, \theta, \mathscr{Z}, \mathscr{T}) = \mathscr{U}_{\mathscr{Z}0}(\mathscr{R}, \theta, \mathscr{T}) \tag{7c}$$

The radial, circumferential, and transverse displacements along the $\mathscr{R}$, θ, and $\mathscr{Z}$ axes are denoted by $\mathscr{U}_{\mathscr{R}}$, $\mathscr{U}_{\theta}$, and $\mathscr{U}_{\mathscr{Z}}$, respectively. The terms $\mathfrak{T}_{\mathscr{R}}$ and $\mathfrak{T}_{\theta}$ denote the rotation of the plate's cross-section around the θ-axis and the $\mathscr{R}$-axis, respectively. The hyperbolic functions $\mathbb{f}(\mathscr{Z})$ and $\mathbb{g}(\mathscr{Z})$, which are used in Mechab theory [58], are represented in Eqs. (8a) and (8b). Notably, the terms $\mathscr{U}_{\mathscr{R}0}$, $\mathscr{U}_{\theta 0}$, and $\mathscr{U}_{\mathscr{Z}0}$ correspond to mid-plane displacements along the $\mathscr{R}$, θ, and $\mathscr{Z}$ axes.

$$\mathbb{f}(\mathscr{Z})=\frac{\cosh(\pi/2)}{\cosh(\pi/2)-1}\mathscr{Z}-\frac{\mathrm{h}/\pi}{\cosh(\pi/2)-1}\sinh(\pi\mathscr{Z}/h) \tag{8a}$$

$$\mathbb{g}(\mathscr{Z})=\mathbb{f}(\mathscr{Z})-\mathscr{Z} \tag{8b}$$

$\mathscr{Z}$ is the transverse coordinate in the general cylindrical coordinate of the composite plate in Eqs. (8a) and (8b). The plate hypothesis states that there should be no regular out-of-plane stress. Furthermore, since it is so little and insignificant, it is also presumed that there is no regular out-of-plane strain. If not, there will be thickness locking. The remaining strains with respect to the higher-order shear deformation theory and based on the cylindrical coordinate are [59]:

$$\mathscr{E}_{\mathscr{R}\mathscr{R}}=\frac{\partial\mathscr{U}_{\mathscr{R}0}}{\partial\mathscr{R}}+\mathbb{f}(\mathscr{Z})\frac{\partial\mathfrak{T}_{\mathscr{R}}}{\partial\mathscr{R}}+\mathbb{g}(\mathscr{Z})\frac{\partial^2\mathscr{U}_{\mathscr{Z}0}}{\partial\mathscr{R}^2}+\frac{1}{2}\left(\frac{\partial\mathscr{U}_{\mathscr{Z}0}}{\partial\mathscr{R}}\right)^2 \tag{9a}$$

$$\begin{aligned}\mathscr{E}_{\theta\theta}=&\frac{\partial\mathscr{U}_{\theta 0}}{\mathscr{R}\partial\theta}+\frac{\mathscr{U}_{\mathscr{R}0}}{\mathscr{R}}+\mathbb{f}(\mathscr{Z})\left(\frac{\partial\mathfrak{T}_{\theta}}{\mathscr{R}\partial\theta}+\frac{\mathfrak{T}_{\mathscr{R}}}{\mathscr{R}}\right)+\mathbb{g}(\mathscr{Z})\left(\frac{\partial^2\mathscr{U}_{\mathscr{Z}0}}{\mathscr{R}^2\partial\theta^2}\right.\\&\left.+\frac{\partial\mathscr{U}_{\mathscr{Z}0}}{\mathscr{R}\partial\mathscr{R}}\right)+\frac{1}{2\mathscr{R}^2}\left(\frac{\partial\mathscr{U}_{\mathscr{Z}0}}{\partial\theta}\right)^2\end{aligned} \tag{9b}$$

$$\begin{aligned}\mathfrak{U}_{\mathscr{R}\theta}=&\frac{\partial\mathscr{U}_{\mathscr{R}0}}{\mathscr{R}\partial\theta}+\frac{\partial\mathscr{U}_{\theta 0}}{\partial\mathscr{R}}-\frac{\mathscr{U}_{\theta 0}}{\mathscr{R}}+\mathbb{f}(\mathscr{Z})\left(\frac{\partial\mathfrak{T}_{\mathscr{R}}}{\mathscr{R}\partial\theta}+\frac{\partial\mathfrak{T}_{\theta}}{\partial\mathscr{R}}\right.\\&\left.-\frac{\mathfrak{T}_{\theta}}{\mathscr{R}}\right)+2\mathbb{g}(\mathscr{Z})\left(\frac{\partial^2\mathscr{U}_{\mathscr{Z}0}}{\mathscr{R}\partial\theta\partial\mathscr{R}}-\frac{\partial\mathscr{U}_{\mathscr{Z}0}}{\mathscr{R}^2\partial\theta}\right)+\frac{1}{\mathscr{R}}\frac{\partial\mathscr{U}_{\mathscr{Z}0}}{\partial\mathscr{R}}\frac{\partial\mathscr{U}_{\mathscr{Z}0}}{\partial\theta}\end{aligned} \tag{9c}$$

$$\mathfrak{U}_{\mathscr{R}\mathscr{Z}}=\frac{\partial\mathbb{f}(\mathscr{Z})}{\partial\mathscr{Z}}\left(\mathfrak{T}_{\mathscr{R}}+\frac{\partial\mathscr{U}_{\mathscr{Z}0}}{\partial\mathscr{R}}\right) \tag{9d}$$

$$\mathfrak{U}_{\theta\mathscr{Z}}=\frac{\partial\mathbb{f}(\mathscr{Z})}{\partial\mathscr{Z}}\left(\mathfrak{T}_{\theta}+\frac{\partial\mathscr{U}_{\mathscr{Z}0}}{\mathscr{R}\partial\theta}\right) \tag{9e}$$

The transverse shear strains in Eq. (9a-e) are designated by $\mathscr{T}_{\mathscr{R}\mathscr{Z}}$ and $\mathscr{T}_{\theta\mathscr{Z}}$, the in-plane shear strain by $\mathscr{T}_{\mathscr{R}\theta}$, and the in-plane normal strains by $\mathscr{E}_{\mathscr{R}\mathscr{R}}$ and $\mathscr{E}_{\theta\theta}$. The overall relationship between stresses and strains for composite laminated materials is expressed by Hooke's constitutive law, which has the following definition [60]:

$$\begin{Bmatrix}\mathfrak{F}_{\mathscr{R}\mathscr{R}}\\\mathfrak{F}_{\theta\theta}\\\mathfrak{F}_{\theta\mathscr{Z}}\\\mathfrak{F}_{\mathscr{R}\mathscr{Z}}\\\mathfrak{F}_{\mathscr{R}\theta}\end{Bmatrix}=\begin{bmatrix}\overline{\mathfrak{Y}}_{11j}&\overline{\mathfrak{Y}}_{12j}&0&0&0\\\overline{\mathfrak{Y}}_{12j}&\overline{\mathfrak{Y}}_{22j}&0&0&0\\0&0&\overline{\mathfrak{Y}}_{44j}&0&0\\0&0&0&\overline{\mathfrak{Y}}_{55j}&0\\0&0&0&0&\overline{\mathfrak{Y}}_{66j}\end{bmatrix}\begin{Bmatrix}\mathscr{E}_{\mathscr{R}\mathscr{R}}\\\mathscr{E}_{\theta\theta}\\\mathfrak{U}_{\theta\mathscr{Z}}\\\mathfrak{U}_{\mathscr{R}\mathscr{Z}}\\\mathfrak{U}_{\mathscr{R}\theta}\end{Bmatrix}.\quad j=b,c,\mathrm{and}\,t \tag{10}$$

In this case, normal in-plane stress is denoted by $\mathfrak{F}_{\mathscr{R}\mathscr{R}}$ and $\mathfrak{F}_{\theta\theta}$, in-plane shear stress by $\mathfrak{F}_{\mathscr{R}\theta}$, and transverse shear stress is denoted by $\mathfrak{F}_{\theta\mathscr{Z}}$ and $\mathfrak{F}_{\mathscr{R}\mathscr{Z}}$. The annular plate's kth polar orthotropic layer is denoted by the superscript k. The arrays of the reduced stiffness matrix, denoted as $\overline{\mathfrak{Y}}_{pq}$, $p,q=1:6$, are expressed as Eqs. (11), (12).

For face-sheets have [60]:

$$\begin{aligned}&\overline{\mathfrak{Y}}_{11b}=\frac{E_b}{1-\vartheta_b^2},\overline{\mathfrak{Y}}_{22b}=\overline{\mathfrak{Y}}_{11b}\\&\overline{\mathfrak{Y}}_{12b}=\frac{\vartheta_b E_b}{1-\vartheta_b^2},\overline{\mathfrak{Y}}_{21b}=\overline{\mathfrak{Y}}_{12b}\\&\overline{\mathfrak{Y}}_{44b}=\frac{E_b}{2(1+\vartheta_b)},\overline{\mathfrak{Y}}_{66b}=\overline{\mathfrak{Y}}_{55b}=\overline{\mathfrak{Y}}_{44b}\\&\overline{\mathfrak{Y}}_{11t}=\frac{E_t}{1-\vartheta_t^2},\overline{\mathfrak{Y}}_{22t}=\overline{\mathfrak{Y}}_{11t}\\&\overline{\mathfrak{Y}}_{12t}=\frac{\vartheta_t E_t}{1-\vartheta_t^2},\overline{\mathfrak{Y}}_{21t}=\overline{\mathfrak{Y}}_{12t}\\&\overline{\mathfrak{Y}}_{44t}=\frac{E_t}{2(1+\vartheta_t)},\overline{\mathfrak{Y}}_{66t}=\overline{\mathfrak{Y}}_{55t}=\overline{\mathfrak{Y}}_{44t}\end{aligned} \tag{11}$$

Also, for the copper core we have [61]:

$$\begin{aligned}&\overline{\mathfrak{Y}}_{11c}=\frac{E_{Cu}}{1-\vartheta_{Cu}^2},\overline{\mathfrak{Y}}_{22c}=\overline{\mathfrak{Y}}_{11c}\\&\overline{\mathfrak{Y}}_{12c}=\frac{\vartheta_{Cu}E_{Cu}}{1-\vartheta_{Cu}^2},\overline{\mathfrak{Y}}_{21c}=\overline{\mathfrak{Y}}_{12c}\\&\overline{\mathfrak{Y}}_{44c}=\frac{E_{Cu}}{2(1+\vartheta_{Cu})},\overline{\mathfrak{Y}}_{66c}=\overline{\mathfrak{Y}}_{55c}=\overline{\mathfrak{Y}}_{44c}\end{aligned} \tag{12}$$

By integrating the stresses across the thickness of the plate, the stress resultants will be derived [62].

$$(\mathscr{n}_{\mathscr{R}\mathscr{R}},\mathscr{n}_{\theta\theta},\mathscr{n}_{\mathscr{R}\theta})=\int_{-\frac{h}{2}}^{-\frac{h_c}{2}}(\mathfrak{F}_{\mathscr{R}\mathscr{R}},\mathfrak{F}_{\theta\theta},\mathfrak{F}_{\mathscr{R}\theta})d\mathscr{Z}+\int_{-\frac{h_c}{2}}^{\frac{h_c}{2}}(\mathfrak{F}_{\mathscr{R}\mathscr{R}},\mathfrak{F}_{\theta\theta},\mathfrak{F}_{\mathscr{R}\theta})d\mathscr{Z}+\int_{\frac{h_c}{2}}^{\frac{h}{2}}(\mathfrak{F}_{\mathscr{R}\mathscr{R}},\mathfrak{F}_{\theta\theta},\mathfrak{F}_{\mathscr{R}\theta})d\mathscr{Z} \tag{13a}$$

$$(\mathscr{m}_{\mathscr{R}\mathscr{R}},\mathscr{m}_{\theta\theta},\mathscr{m}_{\mathscr{R}\theta})=\int_{-\frac{h}{2}}^{-\frac{h_c}{2}}\mathbb{f}(\mathscr{Z})(\mathfrak{F}_{\mathscr{R}\mathscr{R}},\mathfrak{F}_{\theta\theta},\mathfrak{F}_{\mathscr{R}\theta})d\mathscr{Z}+\int_{-\frac{h_c}{2}}^{\frac{h_c}{2}}\mathbb{f}(\mathscr{Z})(\mathfrak{F}_{\mathscr{R}\mathscr{R}},\mathfrak{F}_{\theta\theta},\mathfrak{F}_{\mathscr{R}\theta})d\mathscr{Z}+\int_{\frac{h_c}{2}}^{\frac{h}{2}}\mathbb{f}(\mathscr{Z})(\mathfrak{F}_{\mathscr{R}\mathscr{R}},\mathfrak{F}_{\theta\theta},\mathfrak{F}_{\mathscr{R}\theta})d\mathscr{Z} \tag{13b}$$

$$(\mathscr{p}_{\mathscr{R}\mathscr{R}},\mathscr{p}_{\theta\theta},\mathscr{p}_{\mathscr{R}\theta})=\int_{-\frac{h}{2}}^{-\frac{h_c}{2}}\mathbb{g}(\mathscr{Z})(\mathfrak{F}_{\mathscr{R}\mathscr{R}},\mathfrak{F}_{\theta\theta},\mathfrak{F}_{\mathscr{R}\theta})d\mathscr{Z}+\int_{-\frac{h_c}{2}}^{\frac{h_c}{2}}\mathbb{g}(\mathscr{Z})(\mathfrak{F}_{\mathscr{R}\mathscr{R}},\mathfrak{F}_{\theta\theta},\mathfrak{F}_{\mathscr{R}\theta})d\mathscr{Z}+\int_{\frac{h_c}{2}}^{\frac{h}{2}}\mathbb{g}(\mathscr{Z})(\mathfrak{F}_{\mathscr{R}\mathscr{R}},\mathfrak{F}_{\theta\theta},\mathfrak{F}_{\mathscr{R}\theta})d\mathscr{Z} \tag{13c}$$

4. Equations of motion

This section of the research will develop the laminated annular plates' dynamic equations using Hamilton's principle. Consequently, the following form may be used to express Hamilton's principle in the polar coordinate for the structure [63].

$$\int_{\mathscr{T}_0}^{\mathscr{T}_1}\int_0^{\theta}\int_{R_i}^{R_o} \times \int_{-\frac{h}{2}}^{+\frac{h}{2}}\begin{pmatrix} \rho\left(\dot{\mathscr{U}}_{\mathscr{R}}\delta\dot{\mathscr{U}}_{\mathscr{R}}+\dot{\mathscr{U}}_{\theta}\delta\dot{\mathscr{U}}_{\theta}+\dot{\mathscr{U}}_{\mathscr{Z}}\delta\dot{\mathscr{U}}_{\mathscr{Z}}\right)+F(\mathscr{T})-W_a\mathscr{U}_{\mathscr{Z}0} \\ -(\mathfrak{F}_{\mathscr{R}\mathscr{R}}\delta\mathscr{E}_{\mathscr{R}\mathscr{R}}+\mathfrak{F}_{\theta\theta}\delta\mathscr{E}_{\theta\theta}+\mathfrak{F}_{\mathscr{R}\theta}\delta\mathfrak{U}_{\mathscr{R}\theta}+\mathfrak{F}_{\mathscr{R}\mathscr{Z}}\delta\mathfrak{U}_{\mathscr{R}\mathscr{Z}}+\mathfrak{F}_{\theta\mathscr{Z}}\delta\mathfrak{U}_{\theta\mathscr{Z}})\end{pmatrix} \times\mathscr{R}d\mathscr{Z}\,d\mathscr{R}d\theta d\mathscr{T} = 0 \tag{14}$$

where the opening angle, inner and outer radius, respectively, are introduced by θ, R_i, and R_o. Additionally, the intensity load and excitation frequency are shown by $\mathbb{f}_0$, Ω, and $F(\mathscr{T}) = P\cos(\Omega\mathscr{T})$. Furthermore, $W_a = K_w\mathscr{U}_{\mathscr{Z}0} + D_f\nabla^4\mathscr{U}_{\mathscr{Z}0}$, K_w, $\mathscr{W}_0$, ν_f, and h_f represent the foundation plate thickness, Winkler coefficient, plate deflection, and Poisson's ratio of the auxetic foundation, in that order. D_f is also equivalent to $\frac{E_f h_f^3}{12(1-\nu_f^2)}$. Using Hamilton's principle to apply Eqs. (9a-e), (10), and (13a-d) and the knowledge that $\delta(\mathscr{U}_{\mathscr{R}0}, \mathscr{U}_{\theta0}, \mathscr{U}_{\mathscr{Z}0}, \mathfrak{T}_{\mathscr{R}}, \mathfrak{T}_{\theta})$ at $\mathscr{T} = \mathscr{T}_0$ and $\mathscr{T}_1$ are zero, the dynamic equations in terms of stress resultants will be found in the following relations:

$$\delta\mathscr{U}_{\mathscr{R}0}: \frac{\partial n_{\mathscr{R}\mathscr{R}}}{\partial\mathscr{R}}+\frac{\partial n_{\mathscr{R}\theta}}{\mathscr{R}\partial\theta}+\frac{1}{\mathscr{R}}(n_{\mathscr{R}\mathscr{R}}-n_{\theta\theta}) = i_0\ddot{\mathscr{U}}_{\mathscr{R}0}+i_1\ddot{\mathfrak{T}}_{\mathscr{R}}+i_3\frac{\partial\ddot{\mathscr{U}}_{\mathscr{Z}0}}{\partial\mathscr{R}} \tag{15a}$$

$$\delta\mathscr{U}_{\theta0}: \frac{\partial n_{\theta\theta}}{\mathscr{R}\partial\theta}+\frac{\partial n_{\mathscr{R}\theta}}{\partial\mathscr{R}}+\frac{2n_{\mathscr{R}\theta}}{\mathscr{R}} = i_0\ddot{\mathscr{U}}_{\theta0}+i_1\ddot{\mathfrak{T}}_{\theta}+i_3\frac{\partial\ddot{\mathscr{U}}_{\mathscr{Z}0}}{\mathscr{R}\partial\theta} \tag{15b}$$

$$\begin{aligned}\delta\mathscr{U}_{\mathscr{Z}0}: &\frac{\partial q_{\mathscr{R}\mathscr{Z}}}{\partial\mathscr{R}}+\frac{q_{\mathscr{R}\mathscr{Z}}}{\mathscr{R}}+\frac{\partial q_{\theta\mathscr{Z}}}{\mathscr{R}\partial\theta}-\left(\frac{\partial^2 p_{\mathscr{R}\mathscr{R}}}{\partial\mathscr{R}^2}+2\frac{\partial p_{\mathscr{R}\mathscr{R}}}{\mathscr{R}\partial\mathscr{R}}+\frac{\partial^2 p_{\theta\theta}}{\mathscr{R}^2\partial\theta^2}-\frac{\partial p_{\theta\theta}}{\mathscr{R}\partial\mathscr{R}}+2\frac{\partial^2 p_{\mathscr{R}\theta}}{\mathscr{R}\partial\mathscr{R}\partial\theta}\right.\\ &\left.+2\frac{\partial p_{\mathscr{R}\theta}}{\mathscr{R}^2\partial\theta}\right)+\frac{1}{\mathscr{R}}(r n_{\mathscr{R}\mathscr{R}}\mathscr{U}_{\mathscr{Z}0,\mathscr{R}})_{,\mathscr{R}}+\frac{1}{\mathscr{R}^2}(n_{\theta\theta}\mathscr{U}_{\mathscr{Z}0,\theta})_{\theta}+\frac{1}{\mathscr{R}}(n_{\mathscr{R}\theta}\mathscr{U}_{\mathscr{Z}0,\theta})_{,\mathscr{R}}+\frac{1}{\mathscr{R}}(n_{\mathscr{R}\theta}\mathscr{U}_{\mathscr{Z}0,\mathscr{R}})_{,\theta}-F(\mathscr{T})-K_w\mathscr{U}_{\mathscr{Z}0}+D_f\nabla^4\mathscr{U}_{\mathscr{Z}0}\\ &=-i_3\left(\frac{\partial\ddot{\mathscr{U}}_{\mathscr{R}0}}{\partial\mathscr{R}}-\frac{\ddot{\mathscr{U}}_{\mathscr{R}0}}{\mathscr{R}}\right)-i_4\left(\frac{\partial\ddot{\mathfrak{T}}_{\mathscr{R}}}{\partial\mathscr{R}}-\frac{\ddot{\mathfrak{T}}_{\mathscr{R}}}{\mathscr{R}}\right)-i_3\frac{\partial\ddot{\mathscr{U}}_{\theta0}}{\mathscr{R}\partial\theta}-i_4\frac{\partial\ddot{\mathfrak{T}}_{\theta}}{\mathscr{R}\partial\theta}+i_0\ddot{\mathscr{U}}_{\mathscr{Z}0}-i_5\left(\frac{\partial^2\ddot{\mathscr{U}}_{\mathscr{Z}0}}{\partial\mathscr{R}^2}+\frac{\partial\ddot{\mathscr{U}}_{\mathscr{Z}0}}{\mathscr{R}\partial\mathscr{R}}+\frac{\partial^2\ddot{\mathscr{U}}_{\mathscr{Z}0}}{\mathscr{R}^2\partial\theta^2}\right)\end{aligned} \tag{15c}$$

$$\begin{aligned}\delta\mathfrak{T}_{\mathscr{R}}: &\frac{\partial m_{\mathscr{R}\mathscr{R}}}{\partial\mathscr{R}}+\frac{\partial m_{\mathscr{R}\theta}}{\mathscr{R}\partial\theta}+\frac{1}{\mathscr{R}}(m_{\mathscr{R}\mathscr{R}}-m_{\theta\theta})-q_{\mathscr{R}\mathscr{Z}}\\ &=i_1\ddot{\mathscr{U}}_{\mathscr{R}0}+i_2\ddot{\mathfrak{T}}_{\mathscr{R}}+i_4\frac{\partial\ddot{\mathscr{U}}_{\mathscr{Z}0}}{\partial\mathscr{R}}\end{aligned} \tag{15d}$$

$$\delta\mathfrak{T}_{\theta}: \frac{\partial m_{\theta\theta}}{\mathscr{R}\partial\theta}+\frac{\partial m_{\mathscr{R}\theta}}{\partial\mathscr{R}}+\frac{2m_{\mathscr{R}\theta}}{\mathscr{R}}-q_{\theta\mathscr{Z}} = i_1\ddot{\mathscr{U}}_{\theta0}+i_2\ddot{\mathfrak{T}}_{\theta}+i_4\frac{\partial\ddot{\mathscr{U}}_{\mathscr{Z}0}}{\mathscr{R}\partial\theta} \tag{15e}$$

where,

$$\begin{Bmatrix} i_0\\ i_1\\ i_2\\ i_3\\ i_4\\ i_5\end{Bmatrix} = \int_{-\frac{h}{2}}^{-\frac{h_c}{2}}\rho_b\begin{Bmatrix}1\\ \mathbb{f}(\mathscr{Z})\\ \mathbb{f}^2(\mathscr{Z})\\ \mathbb{g}(\mathscr{Z})\\ \mathbb{f}(\mathscr{Z})\mathbb{g}(\mathscr{Z})\\ \mathbb{g}^2(\mathscr{Z})\end{Bmatrix}d\mathscr{Z}+\int_{-\frac{h_c}{2}}^{\frac{h_c}{2}}\rho_{Cu}\begin{Bmatrix}1\\ \mathbb{f}(\mathscr{Z})\\ \mathbb{f}^2(\mathscr{Z})\\ \mathbb{g}(\mathscr{Z})\\ \mathbb{f}(\mathscr{Z})\mathbb{g}(\mathscr{Z})\\ \mathbb{g}^2(\mathscr{Z})\end{Bmatrix}d\mathscr{Z}+\int_{\frac{h_c}{2}}^{\frac{h}{2}}\rho_t\begin{Bmatrix}1\\ \mathbb{f}(\mathscr{Z})\\ \mathbb{f}^2(\mathscr{Z})\\ \mathbb{g}(\mathscr{Z})\\ \mathbb{f}(\mathscr{Z})\mathbb{g}(\mathscr{Z})\\ \mathbb{g}^2(\mathscr{Z})\end{Bmatrix}d\mathscr{Z} \tag{16}$$

The boundary conditions at curved edges $\mathscr{R} = \mathscr{R}_i, \mathscr{R}_o$

$$\text{Clamped}: \mathscr{U}_{\mathscr{R}0} = \mathscr{U}_{\theta0} = \mathscr{U}_{\mathscr{Z}0} = \frac{\partial\mathscr{U}_{\mathscr{Z}0}}{\partial\mathscr{R}} = \mathfrak{T}_{\mathscr{R}} = \mathfrak{T}_{\theta} = 0 \tag{17}$$

$$\text{Simply}-\text{supported}: \mathscr{U}_{\mathscr{R}0} = \mathscr{U}_{\theta0} = \mathscr{U}_{\mathscr{Z}0} = p_{\mathscr{R}\mathscr{R}} = m_{\mathscr{R}\mathscr{R}} = \mathfrak{T}_{\theta} = 0$$

$$\text{Free}: n_{\mathscr{R}\mathscr{R}} = n_{\mathscr{R}\theta} = \begin{pmatrix} q_{\mathscr{R}\mathscr{Z}}+\frac{\partial p_{\mathscr{R}\theta}}{\mathscr{R}\partial\theta}+n_{\mathscr{R}\mathscr{R}}\mathscr{U}_{\mathscr{Z}0,\mathscr{R}}+\frac{n_{\mathscr{R}\theta}}{\mathscr{R}}\mathscr{U}_{\mathscr{Z}0,\theta}\\ +i_3\ddot{\mathscr{U}}_{\mathscr{R}0}+i_4\ddot{\mathfrak{T}}_x+i_5\frac{\partial\ddot{\mathscr{U}}_{\mathscr{Z}0}}{\partial\mathscr{R}}\end{pmatrix} = p_{\mathscr{R}\mathscr{R}} = m_{\mathscr{R}\mathscr{R}} = m_{\mathscr{R}\theta} = 0$$

The boundary conditions at straight edges $\theta = 0, \beta$

$$\text{Clamped}: \mathscr{U}_{\mathscr{R}0} = \mathscr{U}_{\theta0} = \mathscr{U}_{\mathscr{Z}0} = \frac{\partial\mathscr{U}_{\mathscr{Z}0}}{\partial\theta} = \mathfrak{T}_{\mathscr{R}} = \mathfrak{T}_{\theta} = 0 \tag{18}$$

$$\text{Simply}-\text{supported}: \mathscr{U}_{\mathscr{R}0} = \mathscr{U}_{\theta0} = \mathscr{U}_{\mathscr{Z}0} = p_{\theta\theta} = \mathfrak{T}_{\mathscr{R}} = m_{\theta\theta} = 0$$

$$\text{Free}: n_{\mathscr{R}\theta} = n_{\theta\theta} = \begin{pmatrix} q_{\theta\mathscr{Z}}+\frac{\partial p_{\mathscr{R}\theta}}{\partial\mathscr{R}}+n_{\mathscr{R}\theta}\mathscr{U}_{\mathscr{Z}0,\mathscr{R}}+\frac{n_{\theta\theta}}{\mathscr{R}}\mathscr{U}_{\mathscr{Z}0,\theta}\\ +i_3\ddot{\mathscr{U}}_{\theta0}+i_4\ddot{\mathfrak{T}}_{\theta}+i_5\frac{\partial\ddot{\mathscr{U}}_{\mathscr{Z}0}}{\mathscr{R}\partial\theta}\end{pmatrix} = p_{\theta\theta} = m_{\mathscr{R}\theta} = m_{\theta\theta} = 0$$

5. Numerical solution

The main steps in using the differential quadrature approach to get a numerical solution are described in this section.

5.1. Differential quadrature approach (DQA)

Using DQA, the p^{th} derivative of $\mathscr{F}(\mathscr{R})$ as a given one-dimensional function would be declared as [64–66].

$$\frac{\partial^p\mathscr{F}(\mathscr{R})}{\partial\mathscr{R}^p} = \sum_{j=1}^{\mathbb{n}_{\mathscr{R}}}\mathscr{A}_{ij}^{(p)}\mathscr{F}(\mathscr{R}_j) for i = 1, 2, \ldots, \mathbb{n}_{\mathscr{R}} \tag{19}$$

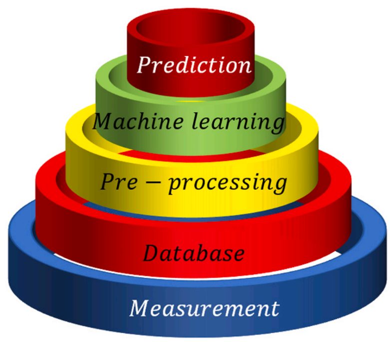

Fig. 3. A flowchart of the presented research to measure nonlinear vibrations of the multi-layer sector plate.

here $\mathscr{A}_{ij}^{(p)}$ represents the weight coefficients for the ith grid point ($j = 1, 2, \ldots, \mathbb{n}_{\mathscr{R}}$) and $\mathbb{n}_{\mathscr{R}}$ is the total number of grid points. According to Eq. (20), $\mathbb{A}_{ij}^{(p)}$ for $i \neq j$ can be derived as [67]:

$$\mathbb{A}_{ij}^{(p)} = p\left(\mathbb{A}_{ii}^{(p-1)}\mathbb{A}_{ij}^{(1)} - \frac{\mathbb{A}_{ij}^{(p-1)}}{\mathscr{R}_i - \mathscr{R}_j}\right), p = 2, 3, \ldots, \mathbb{n}_{\mathscr{R}} - 1 and i, j = 1, 2, \ldots, \mathbb{n}_{\mathscr{R}} \tag{20}$$

here $A_{ij}^{(1)}$ can be acquired by subsequent equation

$$\mathbb{A}_{ij}^{(1)} = \frac{\mathbb{M}^{(1)}(\mathscr{R}_i)}{(\mathscr{R}_i - \mathscr{R}_j)\mathbb{M}^{(1)}(\mathscr{R}_j)}, i, j = 1, 2, \ldots, \mathbb{n}_{\mathscr{R}} \tag{21}$$

Next equation will be employed to determine $\mathbb{A}_{ij}^{(p)}$

$$\mathbb{A}_{ii}^{(p)} = -\sum_{j=1, j\neq i}^{\mathbb{n}_{\mathscr{R}}} \mathbb{A}_{ij}^{(p)}, i = 2, 3, \ldots, \mathbb{n}_{\mathscr{R}} and p = 1, 2, \ldots, \mathbb{n}_{\mathscr{R}} - 1 \tag{22}$$

$\mathbb{M}^{(1)}$ in Eq. (21) can be derived as

$$\mathbb{M}^{(1)}(\mathscr{R}_k) = -\sum_{j=1, j\neq k}^{\mathbb{n}_{\mathscr{R}}} (\mathscr{R}_k - \mathscr{R}_j), for k = 1, 2, 3, \ldots, \mathbb{n}_{\mathscr{R}} \tag{23}$$

5.2. Two-dimensional approximation

The DQA allows for the derivation of the first two derivatives of a given two-dimensional function $\mathscr{F}(\mathscr{R}, \theta)$ [68].

$$\left.\frac{\partial \mathscr{F}}{\partial \mathscr{R}}\right|_{\mathscr{R}=\mathscr{R}_i, \theta=\theta_j} = \sum_{p=1}^{\mathbb{n}_{\mathscr{R}}} \sum_{k=1}^{\mathbb{n}_{\theta}} \mathbb{A}_{ip}^{\mathscr{R}} \imath_{pk}^{\theta} \mathscr{F}_{kj} \tag{24a}$$

$$\left.\frac{\partial \mathscr{F}}{\partial \theta}\right|_{\mathscr{R}=\mathscr{R}_i, \theta=\theta_j} = \sum_{p=1}^{\mathbb{n}_{\mathscr{R}}} \sum_{k=1}^{\mathbb{n}_{\theta}} \imath_{ip}^{\mathscr{R}} \mathbb{A}_{pk}^{\theta} \mathscr{F}_{kj} \tag{24b}$$

$$\frac{\partial}{\partial \mathscr{R}}\left(\left.\frac{\partial \mathscr{F}}{\partial \theta}\right|_{\mathscr{R}=\mathscr{R}_i, \theta=\theta_j}\right) = \sum_{p=1}^{\mathbb{n}_{\mathscr{R}}} \sum_{k=1}^{\mathbb{n}_{\theta}} \mathbb{A}_{ip}^{\mathscr{R}} \mathbb{A}_{pk}^{\theta} \mathscr{F}_{kj} \tag{24c}$$

$$\left.\frac{\partial^2 \mathscr{F}}{\partial \mathscr{R}^2}\right|_{\mathscr{R}=\mathscr{R}_i, \theta=\theta_j} = \sum_{p=1}^{\mathbb{n}_{\mathscr{R}}} \sum_{k=1}^{\mathbb{n}_{\theta}} \mathbb{B}_{ip}^{\mathscr{R}} \imath_{pk}^{\theta} \mathscr{F}_{kj} \tag{24d}$$

$$\left.\frac{\partial^2 \mathscr{F}}{\partial \theta^2}\right|_{\mathscr{R}=\mathscr{R}_i, \theta=\theta_j} = \sum_{p=1}^{\mathbb{n}_{\mathscr{R}}} \sum_{k=1}^{\mathbb{n}_{\theta}} \imath_{ip}^{\mathscr{R}} \mathbb{B}_{pk}^{\theta} \mathscr{F}_{kj} \tag{24e}$$

Here $\mathbb{A}_{pk}^{\theta}$, $\mathbb{A}_{ip}^{\mathscr{R}}$, $\mathbb{B}_{pk}^{\theta}$, and $\mathbb{B}_{ip}^{\mathscr{R}}$ are corresponding weight coefficients. Also, $\mathbb{n}_{\theta}$, and $\mathbb{n}_{\mathscr{R}}$ shows the number of grid points considered through the $\theta -$ and $\mathscr{R} -$ directions. It must be mentioned that $\imath_{ip}^{\mathscr{R}}$, $\imath_{pk}^{\theta}$, $\imath_{ip}^{\mathscr{R}}$, and $\imath_{pk}^{\theta}$ represent identity tensors. By using the Chebyshev–Gauss–Lobatto function, the polar coordination of the grid points $(\mathscr{R}_i, \theta_j)$ maybe obtained in the following manner [69].

$$\mathscr{R}_i = \mathscr{R}_i + \frac{\mathscr{R}_o - \mathscr{R}_i}{2}\left(1 - \cos\left(\frac{(i-1)}{(\mathbb{n}_{\mathscr{R}} - 1)}\pi\right)\right) i = 1, 2, 3, \ldots, \mathbb{n}_{\mathscr{R}} \tag{25a}$$

$$\theta_j = \frac{\beta}{2}\left(1 - \cos\left(\frac{(j-1)}{(\mathbb{n}_{\theta} - 1)}\pi\right)\right) j = 1, 2, 3, \ldots, \mathbb{n}_{\theta} \tag{25b}$$

Using Eqs. (17), (18) for different boundary conditions and Eqs. (24a-e), and (13a-d), (16) for Eq. (15a-e), we obtain:

$$\mathscr{M}\ddot{\mathscr{d}} + [\mathscr{K}_L + \mathscr{K}_{NL}(\mathscr{d})]\mathscr{d} = \mathscr{F} \tag{26}$$

where the mass matrix $\mathscr{M}$, the linear stiffness matrix $\mathscr{K}_L$, and the nonlinear stiffness matrix $\mathscr{K}_{NL}$ are, respectively. The displacement vector $\mathscr{d} = \left\{\mathscr{U}_{\mathscr{R}0ij}^{T}, \mathscr{U}_{\theta 0ij}^{T}, \mathscr{U}_{\mathscr{Z}0ij}^{T}, \mathfrak{T}_{\mathscr{R}ij}^{T}, \mathfrak{T}_{\theta ij}^{T}\right\}^{T}, (i = j = 1, 2, \ldots, \mathbb{n}_{\mathscr{R}} \times \mathbb{n}_{\theta})$ is not known, and the force vector $\mathscr{F}$ resulting from the dynamic load applied is expressed as

$$\mathscr{F} = \left\{\{0\}_{\mathbb{n}_{\mathscr{R}} \times \mathbb{n}_{\theta} \times 1}^{T}, \{0\}_{\mathbb{n}_{\mathscr{R}} \times \mathbb{n}_{\theta} \times 1}^{T}, \{F_0 \cos(\Omega t)\}_{\mathbb{n}_{\mathscr{R}} \times \mathbb{n}_{\theta} \times 1}^{T}, \{0\}_{\mathbb{n}_{\mathscr{R}} \times \mathbb{n}_{\theta} \times 1}^{T}, \{0\}_{\mathbb{n}_{\mathscr{R}} \times \mathbb{n}_{\theta} \times 1}^{T}\right\}^{T} \tag{27}$$

To address the existing dynamic vibration issue, we have chosen to use Newmark's time integration technique to calculate the current problem. The following are the steps to follow:

Algorithm. (START).

Step 1 First computation

1.1 $\boldsymbol{\mathcal{K}} = \boldsymbol{\mathcal{K}}_L$;

1.2 $\ddot{\boldsymbol{d}}_0 = \boldsymbol{\mathcal{M}}^{-1}(\boldsymbol{\mathcal{F}}_0 - \boldsymbol{\mathcal{K}}\boldsymbol{d}_0)$

1.3 Choose the time step ΔT;

1.4 $a_0 = \frac{1}{\beta(\Delta\mathcal{T})^2}, a_1 = \frac{\gamma}{\beta\Delta\mathcal{T}}, a_2 = \frac{1}{\beta\Delta\mathcal{T}}, a_3 = \frac{1}{2\beta} - 1, a_4 = \frac{\gamma}{\beta} - 1, a_5 = \frac{\Delta\mathcal{T}}{2}(\frac{\gamma}{\beta} - 2), a_6 = \Delta\mathcal{T}(1 - \gamma), a_7 = \gamma\Delta\mathcal{T}$;

Step 2 Determine the outcomes at every time step $\mathcal{T}s = 1, 2, \ldots, \mathcal{T}/\Delta\mathcal{T}$

2.1 $\widehat{\boldsymbol{\mathcal{K}}} = \boldsymbol{\mathcal{K}} + \frac{1}{\beta(\Delta\mathcal{T})^2}\boldsymbol{\mathcal{M}}$

2.2 $\widehat{\boldsymbol{\mathcal{F}}}_{\mathcal{T}s} = \boldsymbol{\mathcal{F}}_{\mathcal{T}s} + \boldsymbol{\mathcal{M}}(a_0\boldsymbol{d}_{\mathcal{T}s-1} + a_2\dot{\boldsymbol{d}}_{\mathcal{T}s-1} + a_3\ddot{\boldsymbol{d}}_{\mathcal{T}s-1})$;

2.3 $\boldsymbol{d}_{\mathcal{T}s} = \widehat{\boldsymbol{\mathcal{K}}}^{-1}\widehat{\boldsymbol{\mathcal{F}}}_{\mathcal{T}s}$

2.4 Update and store the acceleration, velocity, and displacement as

$\ddot{\boldsymbol{d}}_{\mathcal{T}s} = a_0(\boldsymbol{d}_{\mathcal{T}s} - \boldsymbol{d}_{\mathcal{T}s-1}) - a_2\dot{\boldsymbol{d}}_{\mathcal{T}s-1} - a_3\ddot{\boldsymbol{d}}_{\mathcal{T}s-1}$

$\dot{\boldsymbol{d}}_{\mathcal{T}s} = \dot{\boldsymbol{d}}_{\mathcal{T}s-1} + a_6\ddot{\boldsymbol{d}}_{\mathcal{T}s-1} + a_7\ddot{\boldsymbol{d}}_{\mathcal{T}s}$

Step 3 The following step involves repeating steps 2.1–2.4 after submitting $\boldsymbol{d}_{\mathcal{T}s}$ into $\boldsymbol{\mathcal{K}}_{NL}(\boldsymbol{d}_{\mathcal{T}s})$ and setting $\boldsymbol{\mathcal{K}} = \boldsymbol{\mathcal{K}}_L + \boldsymbol{\mathcal{K}}_{NL}(\boldsymbol{d}_{\mathcal{T}s})$. $\mathcal{T}s$ is then replaced by $\mathcal{T}s + 1$.

(END)

In the context of Newmark's temporal integration method, all numerical calculations use the constant average acceleration approach with $\beta = 0.25$ and $\gamma = 0.5$. Furthermore, dimensionless quantities are described by

$$\overline{\mathcal{U}}_{\mathcal{Z}} = \frac{\mathcal{U}_{\mathcal{Z}}}{h} \tag{28}$$

6. Introducing artificial intelligence algorithm for nonlinear issues

A flowchart of the current research to estimate nonlinear vibrations of the current problem is presented in Fig. 3.

Hybrid Evolutionary Algorithms (HEAs) that combine Genetic Programming (GP) with neural networks are powerful tools for tackling nonlinear problems, particularly those involving complex mathematical datasets. This combination leverages the strengths of both GP and neural networks: GP's ability to evolve symbolic representations of solutions and neural networks' capability to model complex, high-dimensional data.

6.1. Overview of hybrid evolutionary algorithms (HEAs)

6.1.1. Genetic programming (GP)

GP is an evolutionary algorithm-based methodology inspired by biological evolution to find computer programs that perform a user-defined task. It evolves a population of candidate solutions represented as tree structures, which can be mathematical expressions or symbolic programs.

6.1.2. Neural networks (NNs)

NNs are computational models inspired by the human brain, consisting of interconnected layers of nodes (neurons) that process data. They excel at capturing intricate patterns and relationships in large datasets through learning and generalization.

6.2. Combining GP and neural networks

Hybrid Evolutionary Algorithms (HEAs): These algorithms integrate GP and NNs to capitalize on their complementary strengths. In this hybrid approach, GP is used to evolve the structure or parameters of neural networks, or neural networks are employed to refine and optimize the solutions found by GP.

6.3. Key approaches in HEAs combining GP and NNs

1. **Evolving Neural Network Architectures with GP.**

```
import numpy as np
import random
import tensorflow as tf
from deep import base, creator, tools, gp
from sklearn.datasets import make_regression
from sklearn.model_selection import train_test_split
from sklearn.metrics import mean_squared_error
# Step 1: Setup
# Create a synthetic dataset
X, y = make_regression(n_samples=100, n_features=1, noise=0.1, random_state=42)
X_train, X_test, y_train, y_test = train_test_split(X, y, test_size=0.2, random_state=42)
# Define primitive set for GP
pset = gp.PrimitiveSet("MAIN", 1)
pset.addPrimitive(np.add, 2)
pset.addPrimitive(np.subtract, 2)
pset.addPrimitive(np.multiply, 2)
pset.addPrimitive(np.negative, 1)
pset.addEphemeralConstant("rand101", lambda: random.uniform(-1, 1))
pset.renameArguments(ARG0="x")
```

```
# Step 2: Initialization
creator.create("FitnessMin", base.Fitness, weights=(-1.0,))
creator.create("Individual", gp.PrimitiveTree, fitness=creator.FitnessMin)
toolbox = base.Toolbox()
toolbox.register("expr", gp.genHalfAndHalf, pset=pset, min_=1, max_=2)
toolbox.register("individual", tools.initIterate, creator.Individual, toolbox.expr)
toolbox.register("population", tools.initRepeat, list, toolbox.individual)
```

```
# Step 3: Evaluation
def evalSymbReg(individual, X, y):
    func = toolbox.compile(expr=individual)
    predictions = np.array([func(x) for x in X])
    return mean_squared_error(y, predictions),
toolbox.register("compile", gp.compile, pset=pset)
toolbox.register("evaluate", evalSymbReg, X=X_train, y=y_train)
toolbox.register("select", tools.selTournament, tournsize=3)
toolbox.register("mate", gp.cxOnePoint)
toolbox.register("mutate", gp.mutUniform, expr=toolbox.expr, pset=pset)
toolbox.register("expr_mut", gp.genFull, min_=0, max_=2)
toolbox.decorate("mate", gp.staticLimit(key=len, max_value=17))
toolbox.decorate("mutate", gp.staticLimit(key=len, max_value=17))
```

```
# Step 4: Selection and Step 5: Crossover and Mutation def main():
    random.seed(42)
    pop = toolbox.population(n=300)
    hof = tools.HallOfFame(1)
    stats = tools.Statistics(lambda ind: ind.fitness.values)
    stats.register("avg", np.mean)
    stats.register("std", np.std)
    stats.register("min", np.min)
    stats.register("max", np.max)
```

```
    # Step 6: Neural Network Optimization
    def optimize_with_nn(individual):
        func = toolbox.compile(expr=individual)
        model = tf.keras.Sequential([
            tf.keras.layers.Dense(64, activation='relu', input_shape=(1,)),
            tf.keras.layers.Dense(1)  ])
        model.compile(optimizer='adam', loss='mean_squared_error')
        X_eval = np.array([func(x) for x in X_train]).reshape(-1, 1)
        model.fit(X_eval, y_train, epochs=50, verbose=0)
        return model
```

```
# Run the GP algorithm
    algorithms.eaSimple(pop, toolbox, 0.5, 0.2, 40, stats=stats, halloffame=hof, verbose=True)
    # Refine the best solution using a neural network
    best_individual = hof[0]
    best_nn = optimize_with_nn(best_individual)
    # Evaluate on test set
    X_eval_test = np.array([toolbox.compile(expr=best_individual)(x) for x in X_test]).reshape(-
1, 1)
    nn_predictions = best_nn.predict(X_eval_test).flatten()
    test_mse = mean_squared_error(y_test, nn_predictions)
    print("Best GP Individual: ", best_individual)
    print("Test MSE after NN Optimization: ", test_mse)
if __name__ == "__main__":
    main()
```

Fig. 4. Python implementation of a Hybrid Evolutionary Algorithm that combines Genetic Programming with neural networks to estimate a nonlinear problem using a mathematical dataset.

   - GP is used to evolve the topology and hyperparameters of neural networks, such as the number of layers, types of activation functions, and connectivity patterns.
   - This approach can discover novel and effective neural network architectures tailored to specific nonlinear problems.
2. **GP for Feature Extraction and Representation Learning:**
   - GP evolves symbolic expressions or transformations that serve as features for neural networks.
   - These evolved features can capture domain-specific knowledge and improve the neural network's performance on complex datasets.
3. **Hybrid Models for Symbolic Regression:**
   - GP is employed for symbolic regression to evolve mathematical expressions that model the underlying relationships in the data.
   - Neural networks can be used to refine the coefficients of these expressions or to model residuals, enhancing the overall accuracy.
4. **Neural Networks Guided by GP:**
   - GP evolves initial solutions or structures, which are then fine-tuned and optimized using neural networks.
   - This approach allows the combination of GP's exploration capabilities with neural networks' powerful learning algorithms.

6.4. *Application workflow*

1. **Initialization:**
   - Generate an initial population of candidate solutions using GP. These candidates could represent neural network architectures, feature transformations, or mathematical expressions.
2. **Evaluation**:
   - Evaluate each candidate solution by training the neural networks or computing the fitness of evolved expressions on the mathematical dataset.
   - Fitness evaluation involves assessing how well the solution models the nonlinear relationships in the data.
3. **Selection:**
   - Select the best-performing candidates based on their fitness scores.
   - Apply selection methods like tournament selection, roulette wheel selection, or rank-based selection.
4. **Crossover and Mutation:**
   - Apply genetic operators such as crossover (recombination of parent solutions) and mutation (random alterations) to create new offspring.
   - These operations introduce diversity and explore new regions of the solution space.
5. **Iteration:**
   - Iterate through multiple generations, repeatedly applying evaluation, selection, crossover, and mutation.
   - Over successive generations, the population of solutions evolves towards better performance.
6. **Integration and Optimization:**
   - Integrate the evolved solutions with neural networks for further training and optimization.
   - Fine-tune the neural network parameters using gradient-based methods or other optimization techniques.

6.5. *Benefits and applications*

- **Robustness**: The hybrid approach leverages the exploration capabilities of GP and the learning power of neural networks, making it robust for complex nonlinear problems.
- **Flexibility**: GP can evolve diverse solution structures, while neural networks can fine-tune and optimize these solutions.
- **Accuracy**: Combining symbolic regression with neural networks often leads to highly accurate models for mathematical datasets.

Fig. 4 shows the Python implementation of a hybrid evolutionary algorithm that combines genetic programming (GP) with neural networks to estimate a nonlinear problem using a mathematical dataset. This example will use a symbolic regression approach with GP to evolve mathematical expressions and then use a neural network to optimize the parameters of these expressions.

Table 1
A convergence dynamic deflection of the presented DQA for various $\mathscr{R}_o/\mathscr{R}_i$.

$\mathscr{R}_o/\mathscr{R}_i$	$(\mathfrak{m}_{\mathscr{R}}, \mathfrak{m}_\theta)$				
	(7,7)	(9,9)	(11,11)	(13,13)	(15,15)
1.5	0.2695	0.2153	0.1943	0.1943	0.1943
2	0.2896	0.2689	0.2559	0.2559	0.2559
2.5	0.3593	0.3361	0.3215	0.3215	0.3215
3	0.4389	0.4196	0.4003	0.4003	0.4003
3.5	0.5785	0.5696	0.5381	0.5381	0.5381

6.6. *Step-by-step implementation*

1. **Setup**: Import necessary libraries and define the dataset.
2. **Initialization**: Generate an initial population of candidate solutions using GP.
3. **Evaluation**: Evaluate each candidate by fitting it to the data and calculating fitness.
4. **Selection**: Select the best-performing candidates.
5. **Crossover and Mutation**: Apply genetic operators to create new offspring.
6. **Neural Network Optimization**: Refine the best GP-evolved solutions using a neural network.
7. **Iteration**: Repeat the process for a fixed number of generations.
8. **Results**: Output the best solution.

6.7. *Explanation of each step*

1. **Setup:**
   - Import necessary libraries.
   - Generate a synthetic regression dataset and split it into training and testing sets.
   - Define the primitive set for GP, including arithmetic operations and ephemeral constants.
2. **Initialization:**
   - Create the GP individual and population using DEAP (Distributed Evolutionary Algorithms in Python).
3. **Evaluation:**
   - Define a fitness function (evalSymbReg) to evaluate the mean squared error of GP-evolved expressions against the training data.
4. **Selection and Crossover/Mutation:**
   - Use tournament selection to select the best individuals.
   - Apply one-point crossover and uniform mutation to generate new offspring.
5. **Neural Network Optimization:**
   - Define a function to optimize the best GP-evolved individual using a neural network.
   - Train a simple feedforward neural network on the outputs of the GP-evolved expression.
6. **Iteration:**

Table 2
Comparison between the nonlinear bending result of the present solution with those reported by [51,71], for the dimensionless deflection of an isotropic clamped annular sector plate.

	$\frac{\mathscr{R}_i}{\mathscr{R}_o}= 0.05$	$\frac{\mathscr{R}_i}{\mathscr{R}_o}= 0.1$	$\frac{\mathscr{R}_i}{\mathscr{R}_o}= 0.2$
Ref.[51]	0.30596	0.39811	0.56931
Ref.[71]	0.3208	0.4186	0.5976
Present	0.3220	0.4194	0.5985

Table 3
Dimensionless displacements of FG-GPLRC multilayer annular plate under the cosinoidal load.

Boundary conditions		$\frac{\mathscr{U}_{\mathscr{R}}}{h}$	$\frac{\mathscr{U}_{\mathscr{Z}}}{h}$	$\frac{\mathscr{U}_{\theta}}{h}$
SSSS	Ref.[72]	0.7076	−36.154	−0.2284
	Present	0.7077	−36.156	−0.2287
CSCS	Ref.[72]	−0.1891	−14.010	0.4859
	Present	−0.1895	−14.013	0.4860

- o Run the evolutionary algorithm for a fixed number of generations, recording statistics and the best individual in each generation.

7. **Results:**
   - o Output the best GP-evolved expression and evaluate its performance on the test set after optimization with the neural network.

This section demonstrates how to combine Genetic Programming with neural networks to address a nonlinear regression problem using a hybrid evolutionary algorithm. The mathematical formulation of HEAs that combine GP and neural networks for predicting the nonlinear transient deflections of multi-layer sector plate on auxetic concrete foundation is outlined through the following steps:

6.8. Genetic programming component

GP is used to evolve the mathematical model or function that best describes the nonlinear transient deflections of the system. GP searches through a space of possible mathematical expressions $f_{GP}(x)$ and evolves them based on fitness criteria, typically minimizing the prediction error of the system's dynamic response.

6.8.1. GP process

- **Initialization**: Randomly generate an initial population of potential solutions, represented as tree structures for different mathematical expressions.
- **Fitness Function**: Define the fitness function to minimize the error between the predicted transient deflections $\widehat{w}(t)$ from the GP model and the actual observed data $w(t)$. The fitness function can be defined as:

$$\boldsymbol{Fitness} = \frac{\boldsymbol{1}}{\boldsymbol{N}}\sum_{\boldsymbol{i=1}}^{\boldsymbol{N}}(\boldsymbol{w}(\boldsymbol{t_i}) - \boldsymbol{f_{GP}}(\boldsymbol{t_i}))^{\boldsymbol{2}} \tag{29}$$

- **Selection, Crossover, Mutation**: Evolve the population using genetic operators (crossover, mutation) to create new generations of candidate solutions.

6.9. Neural network component

A neural network is integrated into the hybrid model to capture more complex nonlinear interactions that GP might not efficiently represent. The neural network learns from the residual error between the actual nonlinear response and the GP prediction. The NN is trained with the error data $e(t)$:

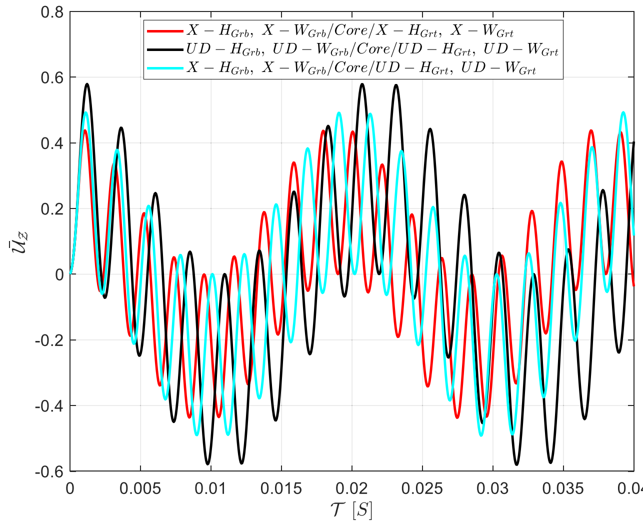

Fig. 5. The influence of the multi-layer structure's distribution pattern and duration of time on the nonlinear transient deflection of the multi-layer sector plate under external excitation.

$$e(t) = w(t) - f_{GP}(t) \tag{30}$$

The neural network then outputs a correction term $f_{NN}(t)$ that refines the GP model:

$$\widehat{w}(t) = f_{GP}(t) + f_{NN}(t) \tag{31}$$

6.10. NN training

The NN model is trained by minimizing the mean squared error between the corrected prediction $\widehat{w}(t)$ and the true response:

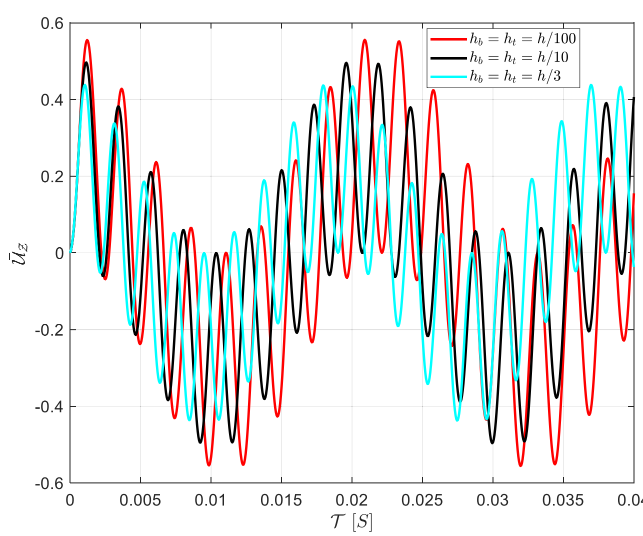

Fig. 6. The impact of duration of time and multi-layer layer's thickness on the transient deflection of the presented structure under external excitation.

Table 4
The time histories of the normalized lateral deflection $\frac{\mathscr{U}_{\mathscr{Z}}}{h}$ ([73]) of SSSS FGM annular sector plates subjected to transient loads for SSSS supported.

	$\frac{c\mathscr{T}}{h}$										
	0	10	20	30	40	50	60	70	80	90	100
Ref.[73]	0	0.0047	0.0021	−0.0038	−0.0032	0.0017	0.0043	0.0003	−0.0047	−0.002	0.0040
Present	0	0.0047	0.0021	−0.0038	−0.0032	0.0017	0.0043	0.0003	−0.0047	−0.002	0.0040

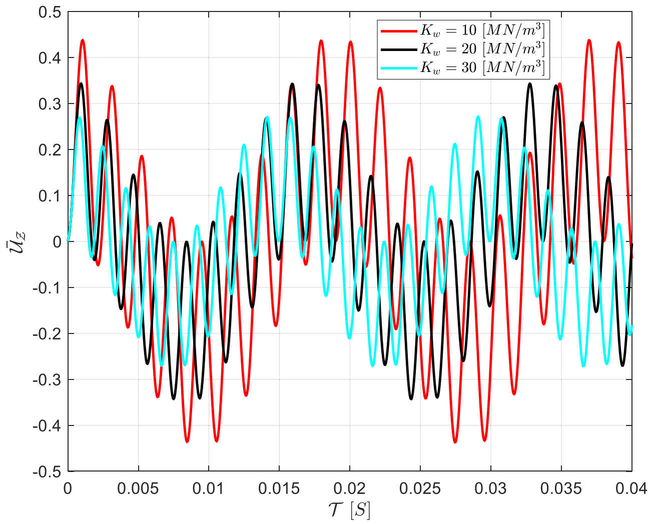

Fig. 7. The impact of duration of time and Winkler coefficient of auxetic concrete foundation on the transient deflection of the presented structure under external excitation.

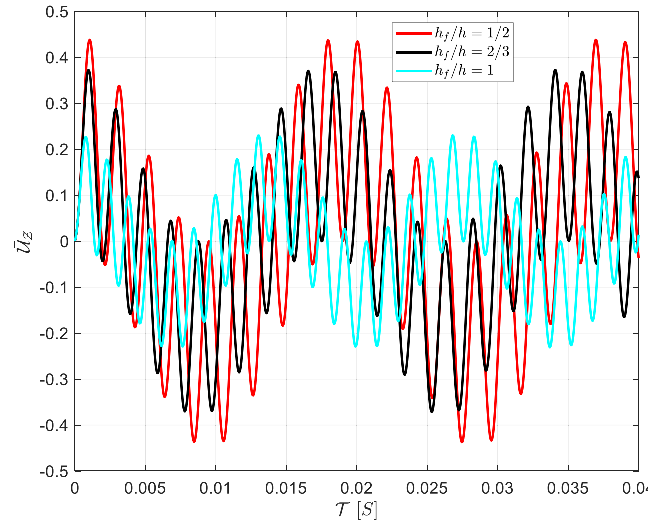

Fig. 9. The influences of the duration of time and thickness ratio of auxetic foundation on the transient deflection of the current multi-layer sector plate under external excitation.

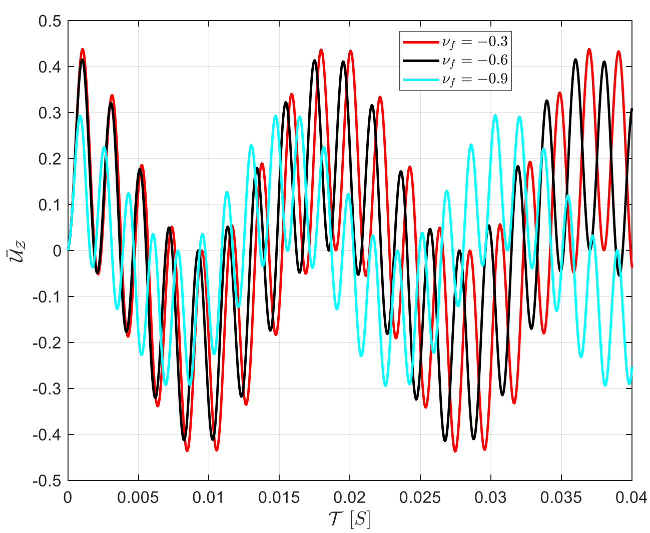

Fig. 8. The influences of the duration of time and Poisson coefficient of auxetic foundation on the transient deflection of the current multi-layer sector plate under external excitation.

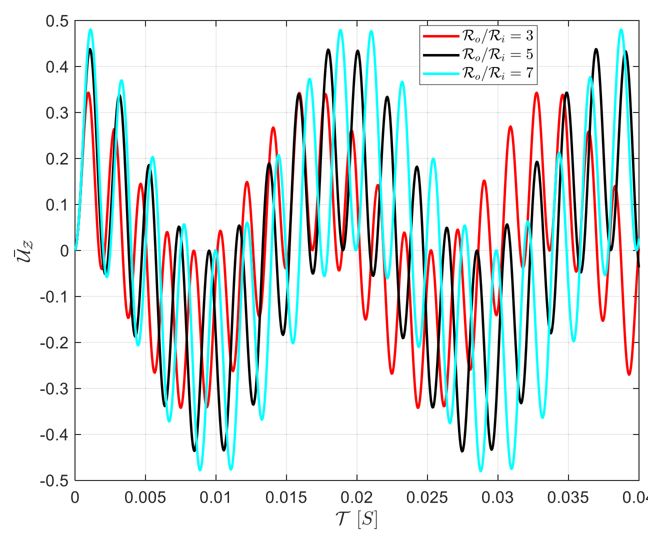

Fig. 10. The impacts of radius ratio and external excitation's duration time on the nonlinear deflection of the current sector plate made of three layers.

$$\boldsymbol{Loss} = \frac{\boldsymbol{1}}{\boldsymbol{N}}\sum_{i=1}^{N}\left(\boldsymbol{w}(\boldsymbol{t_i}) - \widehat{\boldsymbol{w}}(\boldsymbol{t_i})\right)^{\boldsymbol{2}} \tag{32}$$

6.11. Hybrid model for nonlinear transient deflections prediction

The final hybrid model combines the GP and NN outputs:

$$\widehat{w}(t) = f_{GP}(t) + f_{NN}(t) \tag{33}$$

The GP captures the primary transient deflections, while the NN refines the model by addressing the residual complexities. This mathematical framework of HEAs efficiently combines the global approximation power of GP with the local refinement capability of neural networks to predict the nonlinear transient deflections of multi-layer sector plates on auxetic concrete foundation.

7. Results and discussion

In this section, first a verification study between the results of the current study and published articles in the literature to show the accuracy of the current mathematical modeling and solution procedure. In the next subsection, using the mathematical modeling section, the influences of various parameters such as distribution pattern of multi-layer structure, thickness of each multi-layer layer, Winkler coefficient, Poisson and thickness parameters of auxetic foundation, radius ratio, W_{Gr}, H_{Gr}, and external excitation value on the nonlinear dimensionless dynamic deflection of the current problem. The properties of auxetic concrete foundation [70] are $E_f = 25$ [Gpa], and $\vartheta_f = -0.3$. In the last subsection, via the presented artificial inteligence algorithm and the outcomes of mathematical modeling, the trained, validated and tested results of the artificial inteligence algorithm to predict the nonlinear dynamic deflection of the multi-layer structure are presented.

7.1. A convergence study

A convergence study for the presented DQA for various $\mathscr{R}_o/\mathscr{R}_i$ is shown in Table 1. As is observed, eleven node numbers along with $\mathscr{R}$ and θ directions are appropriated for convergence results. Also, from

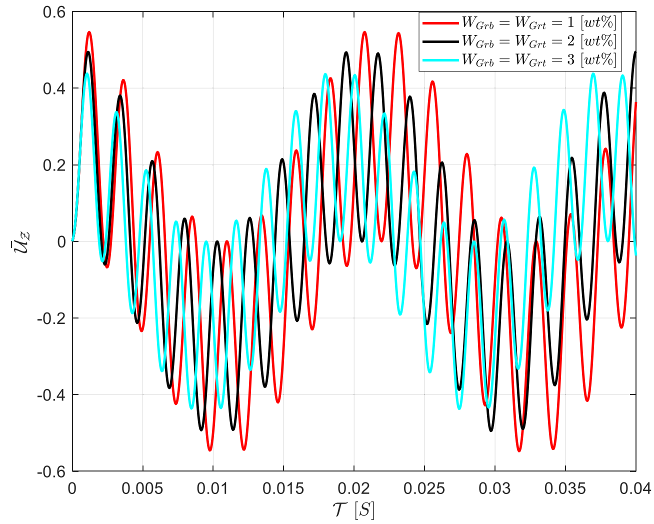

Fig. 11. The impacts of W_{Gr} values of the top and lower layers and external excitation's duration time on the nonlinear deflection of the current sector plate made of three layers.

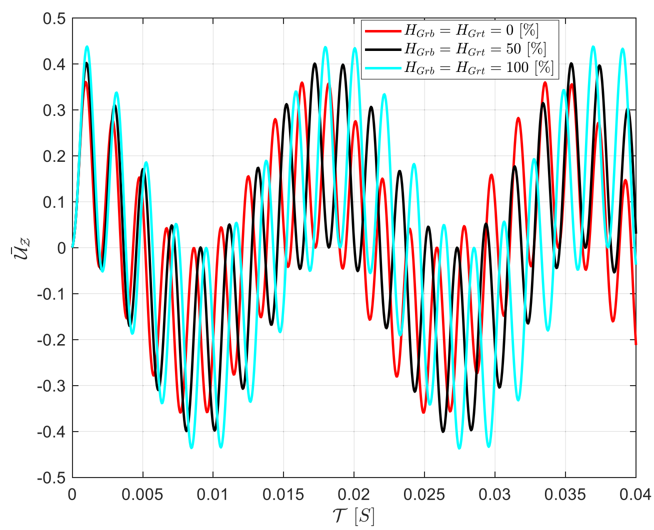

Fig. 12. The impacts of H_{Gr} values of the top and lower layers and external excitation's duration time on the nonlinear deflection of the current sector plate made of three layers.

Table 3 can be seen that increasing the $\mathscr{R}_o/\mathscr{R}_i$ parameter, the dimensionless dynamic deflection of the presented system increases.

7.2. Validation

A verification study is presented to show the accuracy of the current mathematics simulation and solution procedure. In this work by ignoring the influences of auxetic concrete foundation, multi-layer multi-layer structure, and higher-order shear deformation terms, the results can be compared with the outcomes of Refs. [51,71]. As is seen in Table 2, the dimensionless bending results of the clamped annular sector plate structure are compared with the outcomes of Refs. [51,71] for various radius ratios. As is seen, by increasing the radius ratio, due to decreasing the stability in the system, the dynamic deflection of the clamped annular sector plate increases. From Table 2 can be concluded that there is good agreement between the results of current work and published articles in the literature.

Table 3 compares dimensionless displacements of a functionally

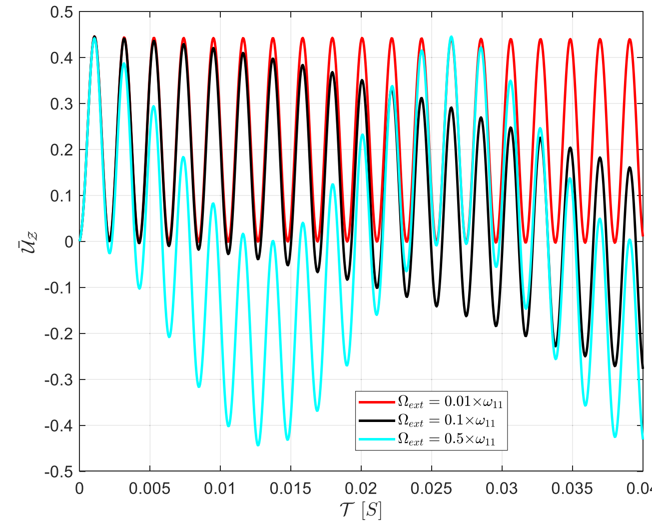

Fig. 13. The influences of time duration and external excitation value on the nonlinear transient deflection change of the current multi-layer sector plate.

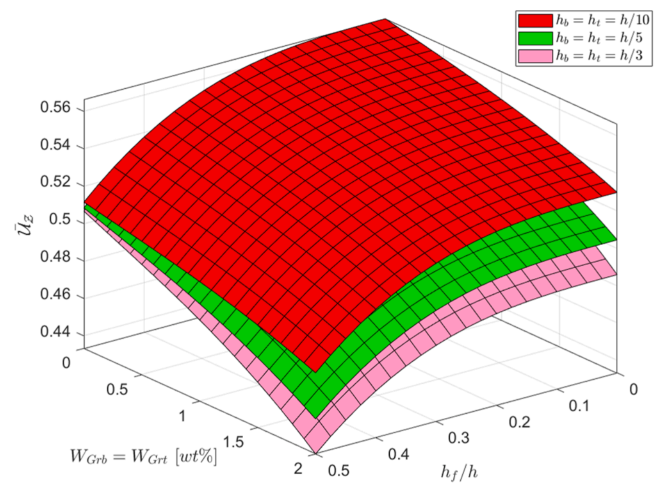

Fig. 14. As a 3D plot, the influences of h_f/h, W_{Gr} on the nonlinear transient deflection for various thicknesses of the layers.

graded graphene platelet-reinforced composite (FG-GPLRC) multilayer annular plate subjected to a cosinoidal load under two types of boundary conditions: simply supported-simply supported (SSSS) and clamped-simply supported-clamped-simply supported (CSCS). The dimensionless displacements

$\mathscr{U}_{\mathscr{R}}/h$, $\mathscr{U}_{\mathscr{Z}}/h$, and $\mathscr{U}_{\theta}/h$ represent radial, axial, and circumferential displacements normalized by the plate thickness. For the SSSS boundary condition, the radial displacement from the reference (Ref. [72]) is 0.7076, while the present study yields a similar result of 0.7077. Similarly, axial displacement and circumferential displacement from both the reference and present study are closely matched. For the CSCS boundary condition, the comparison shows a similar trend, with slight variations in the presented values when compared to the reference. The results from both studies show consistency, validating the present work's accuracy when compared to the reference, with differences only in the fourth decimal place, indicating a high level of agreement between the two studies for the cosinoidal load analysis on FG-GPLRC plates.

Table 4 presents the time histories of normalized lateral deflection of simply supported-simply functionally graded material annular sector plates subjected to transient loads. The results are compared between a reference study (Ref. [73]) and the present work. For each time step, the

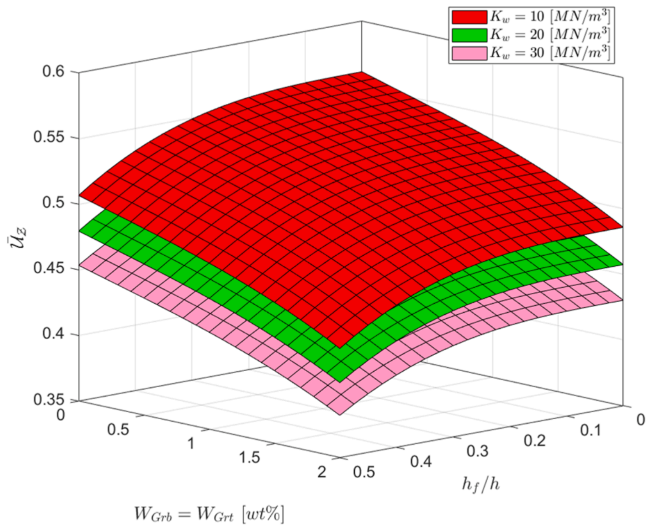

Fig. 15. As a 3D plot, the influences of $\frac{h_f}{h}$, W_{Gr} on the nonlinear transient deflection for various K_w.

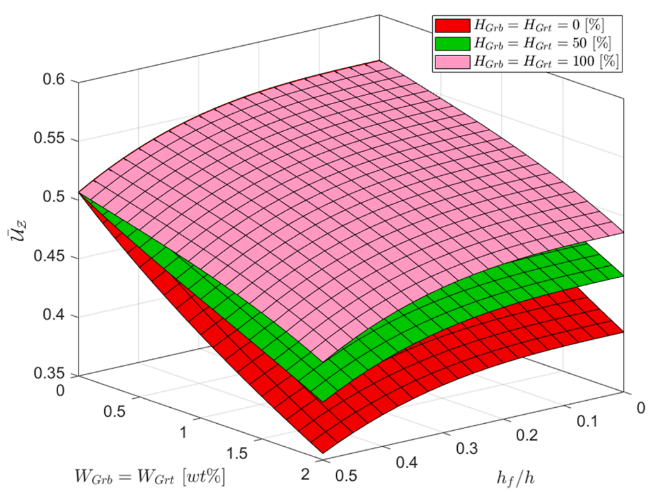

Fig. 16. As a 3D plot, the influences of h_f/h, W_{Gr} on the nonlinear transient deflection for various H_{Gr}.

normalized lateral deflection values are provided. At $c\mathscr{T}/h = 0$, both the reference and present study show zero deflection, indicating the initial state. As time progresses, deflection values fluctuate, reaching maximum and minimum values at different time points. For example, at $c\mathscr{T}/h = 30$, the deflection is negative (-0.0038), while at $c\mathscr{T}/h = 50$, the value is positive (0.0017). The table shows a high degree of consistency between the reference and the present work, with identical results up to the fourth decimal place, confirming the accuracy and reliability of the present analysis in predicting the transient response of SSSS FGM annular sector plates under dynamic loading conditions.

7.3. Parametric results

Fig. 5 shows the influence of the multi-layer structure's distribution pattern and duration of time on the nonlinear transient deflection of the presented multi-layer structure under external excitation. In this figure, $X-H_{Gr}, X-W_{Gr}/Core/X-H_{Gr}, X-W_{Gr}$ is chosen as pattern 1 of the multi-layer structure's distribution pattern. $UD-H_{Gr}, UD-W_{Gr}/Core/UD-H_{Gr}, UD-W_{Gr}$ and $X-H_{Gr}, X-W_{Gr}/Core/UD-H_{Gr}, UD-W_{Gr}$, respectively are selected as pattern 2, and pattern 3 of the multi-layer structure's distribution pattern. As is seen, the distribution pattern has an important role in the nonlinear transient deflection of the multi-layer structure under external excitation. It is clearly seen that, selecting pattern 2 results in the highest nonlinear transient deflection and results in lowest stability than other patterns. Also, selecting Pattern 1 results in the lowest nonlinear transient deflection and highest stability than other patterns. It can be concluded that designers for modeling the current multi-layer system should give careful consideration to the distribution pattern of the multi-layer structure. After applying mechanical excitation on the system, up and down in the nonlinear transient deflection for all patterns can be seen. This up and down of deflection due to mechanical excitation for patterns 1 and 3 are close to each other.

The impact of the duration of time and the multi-layer layer's thickness on the transient deflection of the presented structure under external excitation is shown in Fig. 6. As is seen, selecting a thinner multi-layer structure results in lower stability and higher nonlinear transient deflection than thicker multi-layer structure. This is because, by increasing the thickness, the increase in stiffness in the system is more than mass, and finally, the stability of the system increases. As an amazing result, the influence of thickness on the higher values of duration of time is greater than lower values of time duration. So, in the next figures, the results are obtained via pattern 1 of the multi-layer structure.

The impact of duration of time and Winkler coefficient of auxetic concrete foundation on the transient deflection of the presented structure under external excitation is shown in Fig. 7. As is seen, selecting lower Winkler coefficient results in lower stability and higher nonlinear transient deflection than higher Winkler coefficient. As an amazing result, the influence of thickness on the higher values of duration of time is greater than lower values of time duration.

To know about the influences of the duration of time and Poisson coefficient of auxetic foundation on the transient deflection of the current multi-layer sector plate under external excitation, Fig. 8 appears. As is seen in this figure, by increasing the Poisson coefficient of the auxetic foundation, the stability in the system increases, and finally, the nonlinear transient deflection decreases. This decrease in the higher values of duration of time due to applied external excitation is more clear.

Fig. 9 shows the effects of time length and auxetic foundation thickness ratio on the transient deflection of the current multi-layer sector plate under external stimulation. This figure illustrates how the stability of the system grows and the nonlinear transient deflection eventually diminishes as the auxetic foundation thickness ratio increases. It is more evident how the greater length of time values decreases as a result of applied external stimulation.

The impacts of the radius ratio and external excitation's duration time on the nonlinear deflection of the current sector plate made of three layers is shown in Fig. 10. As is seen, by increasing the radius ratio, the transient deflection and finally the stability in the system increases and decreases, respectively. As an important outcome, the influence of the radius ratio on the transient deflection is not dependent on the value of

```
# Genetic Programming Parameters
population_size = 300
generations = 40
crossover_probability = 0.5
mutation_probability = 0.2
tournament_size = 3
initial_tree_depth = (1, 2)
mutation_tree_depth = (0, 2)
maximum_tree_depth = 17
# Neural Network Parameters
input_neurons = 1
hidden_neurons = 64
output_neurons = 1
activation_function = 'relu'
optimizer = 'adam'
loss_function = 'mean_squared_error'
epochs = 50
```

Fig. 17. A summary of the used parameter values for the algorithm.

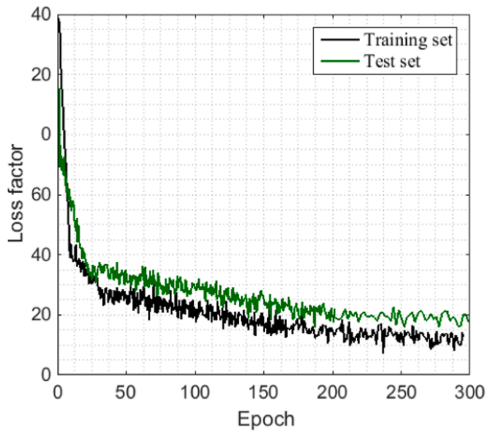

Fig. 18. Loss factor against epoch.

Table 5
An analysis of the amplitude performance of the DNN model at various $\mathscr{R}_o/\mathscr{R}_i$ and RMSN values.

$\mathscr{R}_o/\mathscr{R}_i$	Fit	Predicted		
		$\mathscr{R}MSE_{Train} = 0.81$	$\mathscr{R}MSE_{Train} = 0.89$	$\mathscr{R}MSE_{Train} = 0.91$
1.5	0.3275	0.4112	0.3596	0.3302
2	0.4746	0.5396	0.4862	0.4779
2.5	0.632	0.7493	0.6769	0.6303
3	0.7392	0.837	0.7716	0.7376
3.5	0.8378	0.9476	0.8852	0.839

Table 6
The amplitude performance of the DNN model is assessed over a range of R^2 and $\mathscr{R}_o/\mathscr{R}_i$ values.

$\mathscr{R}_o/\mathscr{R}_i$	Fit	Estimated		
		$R^2 = 0.81529$	$R^2 = 0.93593$	$R^2 = 0.\ 97237$
1.5	0.1943	0.2562	0.2169	0.1967
2	0.2559	0.3219	0.2828	0.2581
2.5	0.3215	0.3883	0.3432	0.3245
3	0.4003	0.4588	0.4219	0.4014
3.5	0.5381	0.6135	0.5664	0.5392

time duration.

The impacts of W_{Gr}values of the toper and lower layers and external excitation's duration time on the nonlinear deflection of the current sector plate made of three layers is shown in Fig. 11. As is seen, by increasing the W_{Gr} values, the transient deflection, and finally the stability in the system decreases and increases, respectively. As an important outcome, the influence of the radius ratio on the transient deflection is highly dependent on the value of time duration. For more clarity, at the higher duration time, the W_{Gr} values have a high influence on the nonlinear deflection of the current sector plate made of three different layers.

Fig. 12 illustrates the effects of the external excitation's duration time and the top and bottom layers H_{Gr}values on the nonlinear deflection of the current sector plate, which is composed of three layers. It is evident that when the H_{Gr} values grow, the system's transient deflection and stability eventually rise and fall, respectively. An important finding is that the value of time duration has a significant impact on the radius ratio's effect on the transient deflection. To be more precise, the nonlinear deflection of the current sector plate, which is composed of three layers, is greatly influenced by the H_{Gr} values at longer duration times.

The influences of time duration and external excitation value on the nonlinear transient deflection change of the current multi-layer sector plate, Fig. 13 is presented. As predicted, by increasing the value of external excitation, an increase in the nonlinear transient deflection can be seen in the system. At the initial time duration, the influence of external excitation value on the nonlinear transient deflection is less than the middle time duration.

As a 3D plot, the influences of h_f/h, W_{Gr} on the nonlinear transient deflection for various thicknesses of the layers, Fig. 14 is presented. As is observed, by increasing the h_f/h the nonlinear transient deflection for all values of W_{Gr} decreases with different slopes. For more detail, in the lower values of W_{Gr}, the influence of h_f/h on the nonlinear transient deflection is less than higher values of W_{Gr}. Also, in the lower values of h_f/h, the influence of the thickness of the layers on the nonlinear transient deflection is more than higher ones. As an important outcome for related industries, in the lower values of W_{Gr}, the influence of the thickness of the layers on the nonlinear transient deflection is less than higher ones.

To know about K_w, W_{Gr} and h_f/h on the nonlinear transient deflection of the multi-layer sector plate surrounded by auxetic concrete foundation appears in Fig. 15. As is seen, by increasing the h_f/h and W_{Gr}, the transient deflection decreases. Also, by increasing the K_w parameter, the nonlinear transient deflection decreases. This decrease in all values of h_f/h and W_{Gr} is the same. For more detail, the influence of K_w parameter on the nonlinear deflection is not dependent on the values of h_f/h and W_{Gr} parameters.

Fig. 16 presents the impacts of h_f/h and W_{Gr} on the nonlinear transient deflection for different HGr as a 3D graphic. It can be shown that for all values of W_{Gr}, the nonlinear transient deflection reduces with varying slopes as the h_f/h increases. More specifically, for lower W_{Gr} levels, h_f/h has less of an impact on the nonlinear transient deflection than at higher W_{Gr} values. Furthermore, the impact of HGr on the nonlinear transient deflection is greater at lower values of h_f/h than at larger ones. A significant finding for linked sectors is that H_{Gr} has less of an impact on the nonlinear transient deflection at lower levels of W_{Gr} than at larger ones.

7.4. The results of trained hybrid deep neural networks

The hybrid evolutionary algorithm combining Genetic Programming (GP) with neural networks is vital for engineering industries tackling complex nonlinear problems. This approach leverages GP's ability to evolve symbolic mathematical expressions, providing interpretable

Table 7
An analysis comparing the outputs of hybrid deep neural networks (HDNN) with mathematical modeling (MM).

W_{Gr} (%)	H_{Gr} (%)							
	0		20		40		60	
	MM	HDNN	MM	HDNN	MM	HDNN	MM	HDNN
0	0.596	0.594	0.610	0.616	0.654	0.647	0.701	0.708
0.5	0.401	0.397	0.593	0.598	0.601	0.595	0.621	0.627
1	0.356	0.352	0.481	0.485	0.521	0.515	0.599	0.605
1.5	0.301	0.298	0.401	0.405	0.492	0.487	0.531	0.536
2	0.281	0.278	0.345	0.348	0.432	0.427	0.490	0.494

models, while neural networks optimize these solutions for accuracy. Such algorithms are essential in fields like predictive maintenance, where accurate modeling of equipment behavior is crucial for preventing failures. In process engineering, they optimize control systems by accurately capturing nonlinear transient deflections, leading to improved efficiency and reduced operational costs. Furthermore, in structural engineering, these algorithms model material properties and structural responses under various conditions, enhancing design robustness and safety. By integrating symbolic regression and deep learning, this hybrid approach offers a powerful tool for solving intricate engineering challenges, driving innovation, and optimizing processes across various engineering domains. Below are the values for the parameters used in the given hybrid evolutionary algorithm:

7.4.1. Genetic programming parameters

1. **Population Size**: 300
   - o The number of candidate solutions (individuals) in the population.
2. **Generations**: 40
   - o The number of iterations (generations) for the evolutionary process.
3. **Crossover Probability**: 0.5
   - o The probability of mating (crossover) between two individuals.
4. **Mutation Probability**: 0.2
   - o The probability of mutating an individual.
5. **Tournament Size**: 3
   - o The number of individuals competing in each tournament for selection.
6. **Primitive Set**:
   - o Operations: Addition, Subtraction, Multiplication, and Negation.
   - o Ephemeral Constants: Random constants uniformly drawn between −1 and 1.
7. **Tree Constraints**:
   - o **Initial Tree Depth**: Between 1 and 2.
   - o **Mutation Tree Depth**: Between 0 and 2.
   - o **Maximum Tree Depth**: 17.

7.4.2. Neural network parameters

1. **Model Architecture**:
   - o **Input Layer**: 1 neuron (input shape of (1,)).
   - o **Hidden Layer**: 64 neurons with ReLU activation.
   - o **Output Layer**: 1 neuron (for regression output).
2. **Optimizer**: Adam
   - o Adaptive Moment Estimation (Adam) optimizer, which adjusts the learning rate during training.
3. **Loss Function**: Mean Squared Error (MSE)
   - o MSE is used to evaluate the difference between predicted and actual values.
4. **Epochs**: 50
   - o The number of times the neural network will iterate over the entire training dataset.
5. **Batch Size**: Not explicitly set, using the default value in the model.

Fig. 17 is a summary of the used parameter values for the algorithm:

These parameters provide a balanced approach for the hybrid evolutionary algorithm, ensuring effective exploration of the solution space and robust optimization of the evolved expressions. Using the 3750 datasets of the mathematical section the loss factor against epoch is presented in Fig. 18.

According to the given choices and the results of scientific modeling, the ready results of hybrid deep neural networks are produced now. The present investigation assesses the feasibility of the model by looking at five factual indicators, including root cruel square error (RMSE) and coefficient of assurance (R^2). This section uses Tables 5 and 6 to examine how R^2 and RMSE affect the results. Higher R^2 and RMSE parameter values for a response might be seen as indicating more precision. It is really helpful to have chosen 3750 tests with RMSE= 0.91, $R^2 = 0.97237$, and other results.

According to Tables 5 and 6, the amplitude of the structure increases as the.

$\mathscr{R}_o/\mathscr{R}_i$ increases for both the DNN and numerical techniques.

Now using the data of Fig. 16 and Tables 5, and 6, a comparison study is presented in Table 6. The results of the hybrid deep neural networks (HDNN) that are shown have been compared with the mathematical modeling (MM) findings in Table 7. The effects of W_{Gr} and H_{Gr} on the dimensionless nonlinear deflection of the sector plate are shown in Table 7. Sector plate dimensionless nonlinear deflection decreases as the W_{Gr} is increased from 0 % to 1 %. The sector plate's dimensionless nonlinear deflection decreases as the W_{Gr} in Table 5 increases. Table 7 data shows that there is a good alignment between the MS and MLS findings.

8. Conclusion

Multi-layer sector plates are lightweight and strong, making them perfect for use in aircraft applications. This is particularly true of those that include graphene origami-enabled auxetic metamaterial face sheets. These structures may be used in satellites, armor, and aircraft parts, where impact protection and weight reduction are vital for efficiency and performance. This study employs a mixed machine learning technique and mathematical simulation to investigate the nonlinear transient deflection of a multi-layer sector plate on an auxetic concrete foundation for the first time. For multi-layer sector plates to function well in engineering applications, it is essential to comprehend and anticipate their nonlinear transient deflections. In order to overcome these issues, this study offers a thorough strategy that incorporates cutting-edge methods. In particular, we present the idea of auxetic metamaterial face sheets enabled by graphene origami, which improve the structures' auxetic behavior and mechanical characteristics. Furthermore, to effectively forecast the nonlinear behavior of these structures under changing loading situations, we offer a hybrid deep neural network architecture that leverages mathematical datasets and machine learning capabilities. To further improve the model's predictive power, the coupled differential quadrature methodology, and Newmark's temporal integration method are used. Our approach provides effective and precise predictive modeling of complex structures by integrating machine learning with conventional numerical methods. This offers significant insights for the design and optimization of multi-layer sector plates and auxetic concrete foundations in engineering applications. The following outcomes are obtained:

- ➢ After applying mechanical excitation on the system, up and down in the nonlinear transient deflection for all patterns can be seen. This up and down of deflection due to mechanical excitation for patterns 1 and 3 are close to each other.
- ➢ The influence of thickness on the higher values of duration of time is greater than the lower values of time duration.
- ➢ By increasing the Poisson coefficient of the auxetic foundation, the stability in the system increases, and finally, the nonlinear transient deflection decreases.
- ➢ The influence of the radius ratio on the transient deflection is not dependent on the value of time duration.
- ➢ At the higher duration time, the W_{Gr} values have a high influence on the nonlinear deflection of the current sector plate made of three different layers.
- ➢ The nonlinear transient deflection of the current sector plate, which is composed of three layers, is greatly influenced by the H_{Gr} values at longer duration times.
- ➢ At the lower values of W_{Gr}, the influence of the thickness of the layers on the nonlinear transient deflection is less than higher ones.

Funding

The research is supported by Shaanxi Provincial Department of Education Service Local Special Research Program Project (23JE019) and Shaanxi Provincial Department of Education Service Local Special Research Program Project (22JE018). The authors extend their appreciation to King Saud University for funding this work through Researchers Supporting Project number (RSPD2024R697), King Saud University, Riyadh, Saudi Arabia.

CRediT authorship contribution statement

Hamed Safarpour: Writing – original draft, Software, Data curation, Conceptualization. **Mohammed El-Meligy:** Conceptualization, Data curation, Resources, Software, Supervision, Writing – review & editing. **Peixi Guo:** Writing – original draft, Software, Resources, Data curation, Conceptualization. **Yao Zhang:** Writing – original draft, Methodology, Investigation, Data curation, Conceptualization. **Kashif Saleem:** Data curation, Formal analysis, Funding acquisition, Investigation, Writing – review & editing. **Yu Xi:** Conceptualization, Data curation, Software, Validation, Writing – review & editing.

Declaration of Competing Interest

The author declare that they have no known competing financial interests or personal relationships that could have appeared to influence the work reported in this paper.

References

[1] Khoram-Nejad ES, Moradi S, Shishehsaz M. Effect of crack characteristics on the vibration behavior of post-buckled functionally graded plates. Structures 2023:181–99.
[2] Civalek Ö, Avcar M. Free vibration and buckling analyses of CNT reinforced laminated non-rectangular plates by discrete singular convolution method. Eng Comput 2022;38:489–521.
[3] Civalek Ö, Dastjerdi S, Akgöz B. Buckling and free vibrations of CNT-reinforced cross-ply laminated composite plates. Mech Based Des Struct Mach 2022;50:1914–31.
[4] Dastjerdi S, Akgöz B, Civalek Ö, Malikan M, Eremeyev VA. On the non-linear dynamics of torus-shaped and cylindrical shell structures. Int J Eng Sci 2020;156:103371.
[5] Sobhani E, Masoodi AR, Civalek Ö. On vibrational-based numerical simulation of a jet engine cowl shell-like structure. Mech Adv Mater Struct 2023;30:4016–27.
[6] Kumar R, Jana P. Vibration response of FG-CNTRC plate resting on non-homogeneous elastic foundation via a closed-form dynamic stiffness formulation. Structures 2023:105203.
[7] Soltani M, Momenian M, Civalek O. Stability analysis of multi-layer double nanobeam-system with varying cross-section interconnected by Kerr-type three-parameter elastic layer. Thin-Walled Struct 2024;204:112249.
[8] Uzun B, Yaylı MÖ, Civalek Ö. An investigation on static, vibration and stability analyses of elastically restrained FG porous Timoshenko nanobeams. Microsyst Technol 2024:1–23.
[9] Khorasani M, Soleimani-Javid Z, Arshid E, Amir S, Civalek Ö. Vibration analysis of graphene nanoplatelets' reinforced composite plates integrated by piezo-electromagnetic patches on the piezo-electromagnetic media. Waves Random Complex Media 2024;34:2394–424.
[10] Uzun B, Yaylı MÖ, Civalek Ö. Vibration of embedded restrained composite tube shafts with nonlocal and strain gradient effects. Acta Mech 2024:1–23.
[11] Han X, Wei C, Hu Q, Liu C, Leng X. Stability analysis and design methods of steel pipe piles under non-uniform corrosion. Structures 2024:106714.
[12] Li Y-D, Yu C-Q, Zhu H-C, Tong J-Z, Tong G-S, Xiao Z-B. Global stability design of concrete-filled corrugated steel tubular columns. Structures 2024:106149.
[13] Fang Y, Zhang J, Su Y, Pan J, Feng K, He C. Efficient reliability assessment of slope stability with insightful sensitivity analysis concerning the safety factor. Structures 2024:106523.
[14] Öztürk HT. Research on optimal solutions and algorithm stability analyses in RC continuous beam problems. Structures 2024:106239.
[15] Hu Y-J, Sheng M, Wen H, Zhu W, Zhu J, Jiang C. Mechanical property measurement at high temperature based on a new disc-shaped specimen. Measurement 2024;234:114824.
[16] Altay M, Aydin H. Parameter optimization, microstructural and mechanical properties of fiber laser lap welds of DP1200 steel sheets. Measurement 2024;235:114822.
[17] Liu J, Cao G, Wang H, Cui C, Liu Z. Development of intelligent methodologies perceiving microstructure and mechanical properties of hot rolled steels. Measurement 2023;221:113526.
[18] Zheng C, Yao Q, Shan C, Li Y, Shang X, Li X, et al. Measurement of uniaxial compression mechanical properties of thermally dried coal samples by energy and fragmentation characteristic analyses. Measurement 2023;207:112363.
[19] Namazinia N, Alibeigloo A, Karimiasl M. Free vibration and static analysis of multi-layer composite plate with auxetic core and GPLRC facing sheets in hygrothermal environment. Forces Mech 2024:100264.
[20] Karimiasl M, Alibeigloo A. Nonlinear bending and vibration analysis of multi-layer plate with graphene reinforced micro composite facing sheets and auxetic honeycomb core in thermal environment. Microsyst Technol 2023;29:1739–55.
[21] Fasihihour N, Abad JMN, Karimipour A, Mohebbi MR. Experimental and numerical model for mechanical properties of concrete containing fly ash: Systematic review. Measurement 2022;188:110547.
[22] Sheng H, Wang P, Tang C, Shi Y, Zheng Y. Microstructure and mechanical properties evaluation of automotive plate steel based on micromagnetic NDT technologies. Measurement 2022;199:111459.
[23] Wang P, Zhang Y, Yao E, Mi Y, Zheng Y, Tang C. Method of measuring the mechanical properties of ferromagnetic materials based on magnetostrictive EMAT characteristic parameters. Measurement 2021;168:108187.
[24] K. Özsoy, Examining mechanical properties of profiles manufactured aluminium extrusion dies using powder bed fusion. Measurement 2021;177:109266.
[25] Bennai R, Atmane HA, Tounsi A. A new higher-order shear and normal deformation theory for functionally graded multi-layer beams. Steel Compos Struct 2015;19:521–46.
[26] Mellal F, Bennai R, Avcar M, Nebab M, Atmane HA. On the vibration and buckling behaviors of porous FG beams resting on variable elastic foundation utilizing higher-order shear deformation theory. Acta Mech 2023;234:3955–77.
[27] Bennai R, Atmane RA, Bernard F, Nebab M, Mahmoudi N, Atmane HA, et al. Study on stability and free vibration behavior of porous FGM beams. Steel Compos Struct Int J 2022;45:67–82.
[28] Atmane RA, Mahmoudi N, Bennai R. Investigation on the dynamic response of porous FGM beams resting on variable foundation using a new higher order shear deformation theory. Steel Compos Struct Int J 2021;39:95–107.
[29] Kehli A, Nebab M, Bennai R, Ait Atmane H, Dahmane M. Dynamic characteristics analysis of functionally graded cracked beams resting on viscoelastic medium using a new quasi-3D HSDT. Mech Adv Mater Struct 2024:1–14.
[30] Hadji L, Bernard F, Madan R, Alnujaie A, Ghazwani MH. Bending and buckling of porous multidirectional functionality graded multi-layer plate. Struct Eng Mech Int J 2023;85:233–46.
[31] Nebab M, Dahmane M, Belqassim A, Atmane HA, Bernard F, Benadouda M, et al. Fundamental frequencies of cracked FGM beams with influence of porosity and Winkler/Pasternak/Kerr foundation support using a new quasi-3D HSDT. Mech Adv Mater Struct 2023:1–13.
[32] Hadji L, Atmane HA, Tounsi A, Mechab I, Adda Bedia E. Free vibration of functionally graded multi-layer plates using four-variable refined plate theory. Appl Math Mech 2011;32:925–42.
[33] Chitour M, Bouhadra A, Bourada F, Mamen B, Bousahla AA, Tounsi A, et al. Stability analysis of imperfect FG multi-layer plates containing metallic foam cores under various boundary conditions. Structures 2024:106021.
[34] Lafi DE, Bouhadra A, Mamen B, Menasria A, Bourada M, Bousahla AA, et al. Combined influence of variable distribution models and boundary conditions on the thermodynamic behavior of FG multi-layer plates lying on various elastic foundations. Struct Eng Mech 2024;89:103.
[35] Zouatnia N, Hadji L. Effect of the micromechanical models on the bending of FGM beam using a new hyperbolic shear deformation theory. Earthq Struct 2019;16:177–83.
[36] Zouatnia N, Hadji L. Static and free vibration behavior of functionally graded multi-layer plates using a simple higher order shear deformation theory. Adv Mater Res 2019;8:313–35.
[37] Tounsi A, Bousahla AA, Tahir SI, Mostefa AH, Bourada F, Al-Osta MA, et al. Influences of different boundary conditions and hygro-thermal environment on the free vibration responses of FGM multi-layer plates resting on viscoelastic foundation. Int J Struct Stab Dyn 2023:2450117.
[38] Tounsi A, Mostefa AH, Bousahla AA, Tounsi A, Ghazwani MH, Bourada F, et al. Thermodynamical bending analysis of P-FG multi-layer plates resting on nonlinear visco-Pasternak's elastic foundations. Steel Compos Struct 2023;49:307–23.
[39] Mudhaffar IM, Chikh A, Tounsi A, Al-Osta MA, Al-Zahrani MM, Al-Dulaijan SU. Impact of viscoelastic foundation on bending behavior of FG plate subjected to hygro-thermo-mechanical loads. Struct Eng Mech Int J 2023;86:167–80.
[40] Bounouara F, Aldosari SM, Chikh A, Kaci A, Bousahla AA, Bourada F, et al. The effect of visco-Pasternak foundation on the free vibration behavior of exponentially graded multi-layer plates with various boundary conditions. Steel Compos Struct Int J 2023;46:367–83.
[41] Amar LHH, Bourada F, Bousahla AA, Tounsi A, Benrahou KH, Albalawi H, et al. Buckling analysis of FG plates via 2D and quasi-3D refined shear deformation theories. Struct Eng Mech Int J 2023;85:765–80.
[42] Bennedjadi M, Aldosari SM, Chikh A, Kaci A, Bousahla AA, Bourada F, et al. Visco-elastic foundation effect on buckling response of exponentially graded multi-layer plates under various boundary conditions. Geomech Eng 2023;32:159.
[43] Zaitoun MW, Chikh A, Tounsi A, Sharif A, Al-Osta MA, Al-Dulaijan SU, et al. An efficient computational model for vibration behavior of a functionally graded multi-layer plate in a hygrothermal environment with viscoelastic foundation effects. Eng Comput 2023;39:1127–41.
[44] Tahir SI, Tounsi A, Chikh A, Al-Osta MA, Al-Dulaijan SU, Al-Zahrani MM. The effect of three-variable viscoelastic foundation on the wave propagation in functionally graded multi-layer plates via a simple quasi-3D HSDT. Steel Compos Struct 2022;42:501.

[45] Bouafia K, Selim MM, Bourada F, Bousahla AA, Bourada M, Tounsi A, et al. Bending and free vibration characteristics of various compositions of FG plates on elastic foundation via quasi 3D HSDT model. Steel Compos Struct Int J 2021;41:487–503.
[46] Kouider D, Kaci A, Selim MM, Bousahla AA, Bourada F, Tounsi A, et al. An original four-variable quasi-3D shear deformation theory for the static and free vibration analysis of new type of multi-layer plates with both FG face sheets and FGM hard core. Steel Compos Struct Int J 2021;41:167–91.
[47] Kobayashi H, Turvey GJ. Elastic small deflection analysis of annular sector Mindlin plates. Int J Mech Sci 1994;36:811–27.
[48] Fallah F, Khakbaz A. On an extended Kantorovich method for the mechanical behavior of functionally graded solid/annular sector plates with various boundary conditions. Acta Mech 2017;228:2655–74.
[49] Turvey G, Salehi M. DR large deflection analysis of sector plates. Comput Struct 1990;34:101–12.
[50] Salehi M, Shahidi A. Large deflection analysis of elastic sector Mindlin plates. Comput Struct 1994;52:987–98.
[51] Nath Y, Sharda HB, Sharma A. Non-linear analysis of moderately thick sector plates. Commun Nonlinear Sci Numer Simul 2005;10:765–78. https://doi.org/10.1016/j.cnsns.2004.03.003.
[52] Golmakani M, Alamatian J. Large deflection analysis of shear deformable radially functionally graded sector plates on two-parameter elastic foundations. Eur J Mech A Solids 2013;42:251–65.
[53] Alinaghizadeh F, Shariati M. Geometrically non-linear bending analysis of thick two-directional functionally graded annular sector and rectangular plates with variable thickness resting on non-linear elastic foundation. Compos Part B Eng 2016;86:61–83.
[54] Alinaghizadeh F, Kadkhodayan M. Large deflection analysis of moderately thick radially functionally graded annular sector plates fully and partially rested on two-parameter elastic foundations by GDQ method. Aerosp Sci Technol 2014;39:260–71.
[55] Zhao S, Zhang Y, Zhang Y, Yang J, Kitipornchai S. Vibrational characteristics of functionally graded graphene origami-enabled auxetic metamaterial beams based on machine learning assisted models. Aerosp Sci Technol 2022;130:107906. https://doi.org/10.1016/j.ast.2022.107906.
[56] Zhao S, Zhang Y, Zhang Y, Zhang W, Yang J, Kitipornchai S. Genetic programming-assisted micromechanical models of graphene origami-enabled metal metamaterials. Acta Mater 2022;228:117791.
[57] Ansari R, Torabi J, Hasrati E. Axisymmetric nonlinear vibration analysis of multi-layer annular plates with FG-CNTRC face sheets based on the higher-order shear deformation plate theory. Aerosp Sci Technol 2018;77:306–19. https://doi.org/10.1016/j.ast.2018.01.010.
[58] Ait Atmane H, Tounsi A, Mechab I, Adda Bedia EA. Free vibration analysis of functionally graded plates resting on Winkler–Pasternak elastic foundations using a new shear deformation theory. Int J Mech Mater Des 2010;6:113–21.
[59] Reddy JN. Theory and Analysis of Elastic Plates and Shells. CRC Press; 2006.
[60] Reddy JN. Mechanics of Laminated Composite Plates and Shells: Theory and Analysis. CRC Press; 2003.
[61] He X, Ding J, Habibi M, Safarpour H, Safarpour M. Non-polynomial framework for bending responses of the multi-scale hybrid laminated nanocomposite reinforced circular/annular plate. Thin-Walled Struct 2021;166:108019. https://doi.org/10.1016/j.tws.2021.108019.
[62] Arefi M, Bidgoli EM-R, Dimitri R, Tornabene F. Free vibrations of functionally graded polymer composite nanoplates reinforced with graphene nanoplatelets. Aerosp Sci Technol 2018;81:108–17.
[63] Zhao T, Bayat MJ, kalhori A, Asemi K. Free vibration analysis of functionally graded multilayer hybrid composite cylindrical shell panel reinforced by GPLs and CNTs surrounded by Winkler elastic foundation. Eng Struct 2024;308:117975. https://doi.org/10.1016/j.engstruct.2024.117975.
[64] Sun L, Hao YX, Zhang W, Li H. Traveling wave vibration and critical rotating speed of rotating porous metal conical shell with elastic boundary conditions. Aerosp Sci Technol 2024;148:109091. https://doi.org/10.1016/j.ast.2024.109091.
[65] Pan Z, Cheng J, Zhao L, Ragab AE. Thermo-dynamic response of multi-directional functionally graded panels resting on an elastic substrate with the aid of data-driven solution. Aerosp Sci Technol 2023;143:108724. https://doi.org/10.1016/j.ast.2023.108724.
[66] Wan PH, Al-Furjan MSH, Kolahchi R. Nonlinear flutter response and reliability of supersonic smart hybrid nanocomposite rupture trapezoidal plates subjected to yawed flow using DQHFEM. Aerosp Sci Technol 2024;145:108862. https://doi.org/10.1016/j.ast.2023.108862.
[67] Forooghi A, Fallahi N, Alibeigloo A, Forooghi H, Rezaey S. Static and thermal instability analysis of embedded functionally graded carbon nanotube-reinforced composite plates based on HSDT via GDQM and validated modeling by neural network. Mech Based Des Struct Mach 2022:1–34.
[68] Rahimi A, Alibeigloo A, Safarpour M. Three-dimensional static and free vibration analysis of graphene platelet–reinforced porous composite cylindrical shell. J Vib Control 2020;26:1627–45. https://doi.org/10.1177/1077546320902340.
[69] Tornabene F, Fantuzzi N, Ubertini F, Viola E. Strong formulation finite element method based on differential quadrature: a survey. Appl Mech Rev 2015;67.
[70] Yang W, Yan G, Awwad EM, Al-Razgan M. AI-based solution on the efficient structural design of the graphene-platelets reinforced concrete ceilings. Mech Adv Mater Struct 2023:1–24.
[71] Mehrabian M, Golmakani ME. Nonlinear bending analysis of radial-stiffened annular laminated sector plates with dynamic relaxation method. Comput Math Appl 2015;69:1272–302. https://doi.org/10.1016/j.camwa.2015.03.021.
[72] Liu D, Li Z, Kitipornchai S, Yang J. Three-dimensional free vibration and bending analyses of functionally graded graphene nanoplatelets-reinforced nanocomposite annular plates. Compos Struct 2019;229:111453.
[73] Liang X, Kou H, Wang L, Palmer AC, Wang Z, Liu G. Three-dimensional transient analysis of functionally graded material annular sector plate under various boundary conditions. Compos Struct 2015;132:584–96.